

A foe-inspired friend: Constructing a tumor tissue-mimicking biomaterial to study intratumoral drug transport

By

Sebastian Gonzalo Huayamares Moreno
B.Sc. in Chemical Engineering, University of Kansas, 2018
B.A. in Mathematics, University of Kansas, 2018

© 2020

Submitted to the graduate degree program in Bioengineering and the Graduate Faculty of the University of Kansas in partial fulfillment of the requirements for the degree of Master of Science.

Chair: Dr. Cory Berkland

Dr. Prajnaparamita Dhar

Dr. Kristi Neufeld

Date Defended: May 7th, 2020

The thesis committee for Sebastian Gonzalo Huayamares Moreno certifies that this is the approved version of the following thesis:

A foe-inspired friend: Constructing a tumor tissue-mimicking biomaterial to study intratumoral drug transport

Chairperson Dr. Cory Berkland

Date Approved: May 7th, 2020

Abstract

The design of an *in vitro* model of the tumor microenvironment and its implementation on drug screening of new anticancer therapies is an active challenge that sits at the interface of biomaterials and cancer biology. As recent clinical successes of human intratumoral therapies stimulate research on intratumoral delivery, a need for an *in vitro* 3D tumor model to screen intratumoral therapies arises. Since the drug formulation is injected directly into the tumor, the biophysics of the tumor microenvironment affecting intratumoral retention must be considered in the design of a tumor model. Fibrotic regions characteristic of solid tumors typically are rich in collagen I fibers. Using shear rheology, tumors with lower collagen density were shown to have a lower stiffness. Similarly, the stiffness of the hyaluronic acid hydrogel models was increased with the addition of collagen fibers to model the bulk biomechanical properties of solid tumors. Hyaluronic acid-based hydrogels were then used as intratumoral injection site simulators to model *in vitro* the retention of glatiramer acetate (GA) and polyethylene glycol (PEG) administered intratumorally. Both compounds were also injected in murine head & neck tumors and their retention was studied *ex vivo* for comparison. Retention of GA in the hydrogels was significantly longer than PEG as expected, which was confirmed in the solid tumors. Finally, the biocompatibility of the designed models was assessed by 3D culturing human head & neck cancer cells. Cancer cell viability in the scaffolds was demonstrated, thus setting ground for future applications to assess intratumoral retention time and bulk biomechanical characteristics of solid tumors.

Acknowledgements

Deciding to come to the University of Kansas to pursue my dream of doing research at the interface of engineering and medicine has been the best choice I made in my life so far. The list of friends, peers and mentors that have supported me during the last 6 years as a Jayhawk in undergraduate and graduate career is immense. It is because of them that this thesis was possible, so I will note a few here.

My most sincere gratitude and appreciation go to my M.S. advisor, Dr. Cory Berkland. He has been the type of mentor that I wish to become one day and inspired me with his integrity and humbleness. Cory taught me how to be a good scientist and professional, and always supported all my decisions no matter how bizarre they seemed, like doing a materials science internship in Germany. Cory, thanks for your guidance and friendship over the last couple of years. Thanks are due to my parents too, Federico Huayamares and Monica Moreno. They allowed me to leave Peru and follow my call when I was 17 and have supported me every single step along the way. Mom, your battle with cancer motivated me to try to contribute to the fight against cancer from an engineer and scientist's perspective, so to you I dedicate this thesis.

Big shout out to the Berkland lab mates who have made my time in the lab enjoyable and adventurous. Jimmy Song, Aric Huang, Aparna Chakravarti, Danny Griffin, Melissa Pressnall, Bryce Stottlemire, Kyle Apley, Stephanie Johnson, Jeannie Salash, Justin Ruffalo, Jon Whitlow, Mary Duncan, Dakota Even, and Jian Qian, my graduate experience would not have been half as good without you. Thank you to Sam Crowl and Vivian Yudistyra, the talented undergraduate students that I had the pleasure and honor to mentor and work with.

I would also like to thank the School of Engineering and the University of Kansas for all the support I had as an undergraduate and graduate student through the 2018-2019 Madison & Lila Self Graduating Senior Fellowship and the KU International Excellence Scholarship for full undergraduate tuition support. Special thanks for Dr. Susan Williams for always listening and giving me great advice during rough times, and all my friends from undergrad; they are my family away from home and I would not have enjoyed my time at KU and Kansas this much without them. I am also grateful for my time as a Graduate Teaching Assistant under the mentorship of Dr. Prajna Dhar and Dr. Kevin Leonard; they taught me how to successfully communicate complex concepts and genuinely care for the students to the point that I am sure I would enjoy the teaching aspect of a career in academia. Thanks to Denise Bridwell, as well as my friends in the program, for supporting me and ensuring my success through the Bioengineering Graduate Program.

Thank you to Dr. Iman Taha and Dominik Grund, my supervisors and mentors in the Fraunhofer Research Institute for Casting, Composite and Processing Technology IGCV in Augsburg, Germany, and the German Academic Exchange Services (DAAD) RISE Professional Scholarship. My time in Fraunhofer helped me grow professionally and culturally, and it is with them that I published as a first author for the first time.

Finally, to my committee members, Dr. Prajna Dhar and Dr. Kristi Neufeld, thank you for your time, mentorship through previous coursework and interactions, and feedback to culminate this thesis.

Table of Contents

Chapter 1: Introduction and literature review	1
1. Introduction.....	1
2. Tumor microenvironment	2
3. Intratumoral transport	5
4. Biomaterials for in vitro modeling of the tumor microenvironment.....	8
a) Types of biomaterials.....	8
b) Types of in vitro tumor models.....	9
c) Hyaluronic acid-based scaffold tumor models for drug screening	10
d) Modeling the tumor’s biomechanical properties.....	11
5. Remarks for this thesis.....	13
Chapter 2: Constructing a tumor tissue-mimicking biomaterial to study intratumoral drug transport	14
1. Introduction.....	14
2. Materials and methods	16
a) Materials	16
b) Methacrylation of hyaluronic acid	17
c) Fluorescent dye-labelling of GA and PEG.....	17
d) Fabrication and imaging of hydrogel scaffolds.....	18
e) Staining of tumor tissue and biomaterial	20
f) Rheological analysis	20
g) <i>In vitro</i> drug release	21
h) Mathematical modeling of diffusion coefficients	22
i) Tumor induction in mouse model	23
j) <i>Ex vivo</i> intratumoral release and imaging of tumors.....	23
k) Statistical analysis.....	24
3. Results.....	25
a) Synthesis and characterization of hydrogel scaffolds	25
b) Relative stiffness analysis of scaffolds and solid tumors through shear rheology	26
c) Scaffolds as <i>in vitro</i> models of tumor injection site to study drug release.....	28
d) Modeling of diffusion coefficients for the <i>in vitro</i> release from reservoir models	32
e) <i>Ex vivo</i> intratumoral release and fluorescent imaging	33
4. Discussion.....	36

5. Conclusions.....	38
Chapter 3: Conclusions and future directions	40
1. Conclusions and challenges	40
2. Future directions and applications	41
a) Cancer cell encapsulation for 3D-culture.....	41
b) Assessment of cell viability	42
c) Future applications and considerations	43
References.....	44

Chapter 1: Introduction and literature review

1. Introduction

Recent clinical successes of human intratumoral (IT) immunotherapies have stimulated a wave of new trials investigating IT therapies alone and in tandem with other immuno-oncology agents. IT delivery refers to the direct injection of a drug/formulation into a tumor. IT therapy offers unique anti-cancer benefits, since direct injection bypasses obstacles encountered during systemic trafficking and tumor penetration.¹ Severe immune-related adverse events associated with systemic delivery of cancer immunotherapies²⁻³ can be reduced by delivering small IT doses.⁴ IT administration of immunostimulants, for example, can work synergistically with checkpoint inhibitors making nonresponsive ‘cold’ tumors ‘hot’ by recruiting and activating tumor infiltrating lymphocytes.⁴⁻⁶ Intuitively, the design of IT therapies is significantly different than that of systemic cancer medications, as these localized interventions aim for retention at the administration site or draining lymph nodes with limited systemic exposure.

In this chapter, features of the tumor microenvironment (TME) are explored while highlighting transport mechanisms involved in IT delivery. Additionally, biomaterials-based *in vitro* models of the TME are reviewed and classified, and their potential for drug screening and modeling the tumor’s biomechanical properties is also addressed. Challenges of a few existing tumor models are reviewed, highlighting the lack of an adequate model for *in vitro* screening of IT delivery. Finally, remarks regarding the technology designed in Chapter 2 are offered to highlight its innovative application in comparison to other existing models.

2. Tumor microenvironment

The TME is heterogeneous between patients, tumor types, and often even within individual tumors. Overall, tumor tissue is typically distinct from normal tissue in that it has poorly organized vasculature with inconsistent vessel diameters and more prevalent branching.⁷ Tumor cell distance from blood vessels can result in restriction of oxygen supply causing hypoxia in portions of the tumor.⁸ The poorly organized vasculature and hypoxic setting creates a microenvironment with increased fluid leakage and elevated interstitial fluid pressure (IFP). Compared to the extravascular space in healthy tissue, tumors tend to have higher extracellular matrix (ECM) density lacking functional lymphatic vessels, which limits interstitial diffusion and the drainage of fluid from the tissue.⁹⁻¹⁰ Collectively, the poorly organized vasculature and increased IFP can decrease uptake of circulating therapeutic molecules, which is correlated with poor prognoses in some cases.⁹

Intracellular pH is similar between tumors and normal tissue, although extracellular pH can be more acidic in tumors.¹¹ Increased extracellular acidity and anaerobic glycolysis alter the pH gradients found in the TME versus healthy tissue.¹¹⁻¹² Higher acidity may increase tumor cell invasion and metastatic potential while also aiding in evasion of immune surveillance.¹³⁻¹⁴ For drugs that rely on passive diffusion to enter cells, the decreased extracellular pH may cause the weakly basic drugs to become ionized, preventing diffusion across membranes.^{11, 15}

Tumor tissue often contains immunosuppressive mechanisms that allow malignant cells to proliferate undetected by the immune system. T-regulatory cells (Tregs) are attracted to the tumor by chemokines and aid in suppressing antigen presenting cells (APCs) that may otherwise stimulate a response against tumor antigens.¹⁶ Additionally, tumor cells can secrete anti-inflammatory and regulatory cytokines (ie TGF β , IL-10) that facilitate cancer growth and directly prevent DC activation. Tumor cells can also limit the expression of co-stimulatory molecules

(MHC II, CD80, CD86), potentially inducing anergy or senescence in infiltrating T cells.¹⁶⁻¹⁷ At the other extreme, overstimulation can cause T-cell exhaustion from chronic exposure to tumor antigen.¹⁸ Finally, tumor cells can downregulate the expression of tumor antigens over time, evading recognition by cytotoxic T-lymphocytes (CTLs).

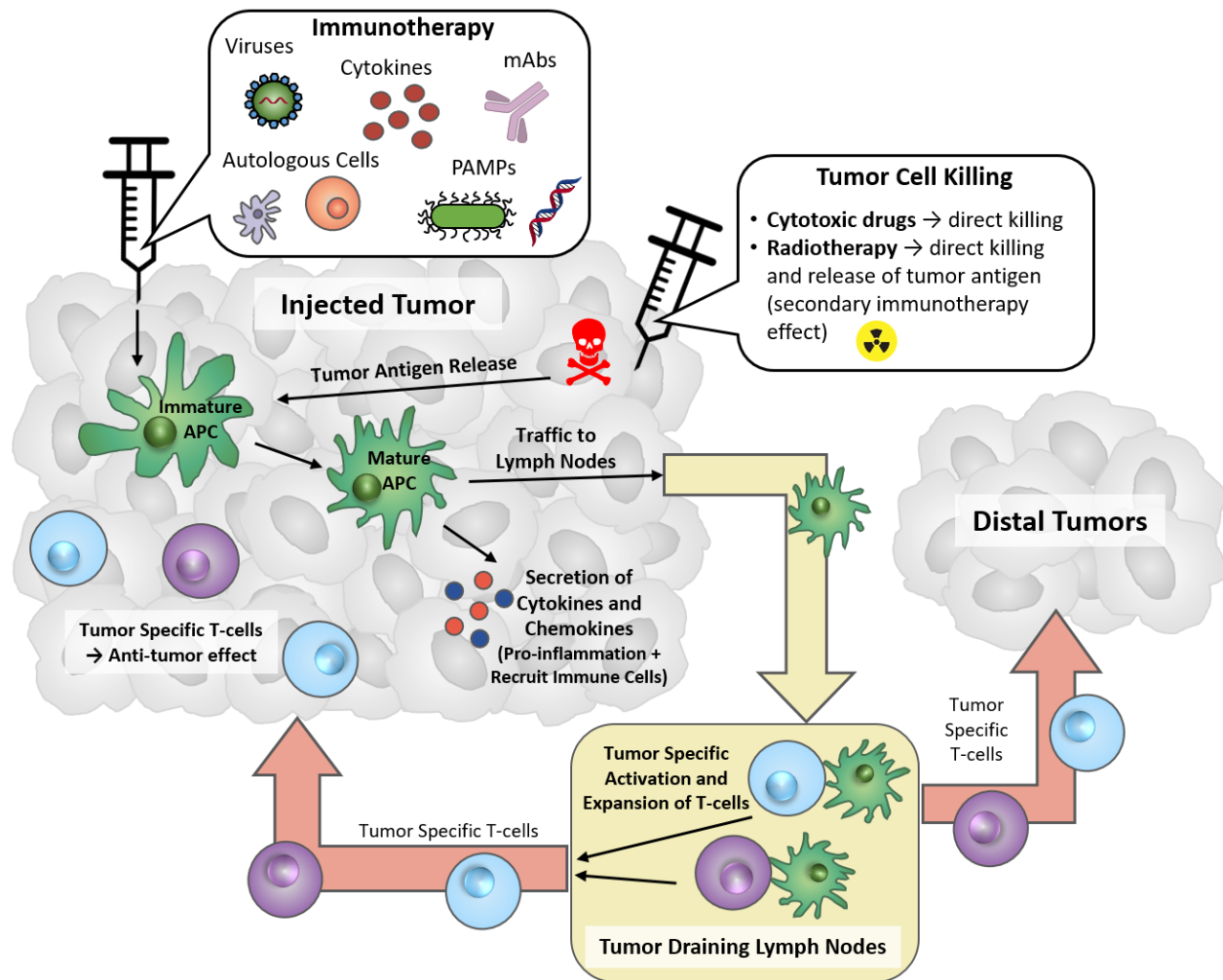


Figure 1. Concept of intratumoral (IT) immunotherapy invoking an abscopal effect. Injection of immunotherapy can activate the innate and adaptive arms of an immune response, leading to systemic effects from circulating adaptive immune cells. See Table 1 for the definition of the various biological agents used as immunotherapy.

Clinical studies indicate that the suppressive environment within the tumor can be overcome with immunostimulants. Immune cells can be activated by immunostimulants in the

presence of tumor antigen, traffic to lymph nodes, and then activate tumor antigen specific T-cells via cross-presentation (**Figure 1**). Antigen-specific T-cells may then circulate back to the tumor or to distal tumors and instigate tumor cell killing. The activation of the innate immune response creates a pro-inflammatory microenvironment and can result in recruitment of additional immune cells to the tumor. Categories of current immunostimulants used in IT cancer therapy are listed in

Table 1.

Table 1. Categories of IT immunostimulants to treat cancer covered in this article.

Category	Mechanism	Cells Types Involved
Pathogen-Associated Molecular Patterns (PAMPs)	<ul style="list-style-type: none"> • Binding toll-like receptors (TLRs), RIG-I-like receptors (RLRs), NOD-like receptors (NLRs), and cell membrane components • Downstream signaling leading to innate immune response 	Immune cells, cancer cells
Cytokines	<ul style="list-style-type: none"> • Binding to specific cell-surface glycoproteins • Downstream signaling leading to innate immune response • Direct anti-proliferative activity 	Immune cells, cancer cells
Viruses and Plasmids	<ul style="list-style-type: none"> • Interaction of viral surface proteins with cell surface proteins • Target cancer cells by exploiting pathways, receptors, and mechanisms that promote tumor growth • Viruses can be used to infect cancer cells or as vehicles for gene delivery • Cell death <i>and</i> downstream signaling leading to innate immune response 	Immune cells, cancer cells
Monoclonal antibodies (mAbs)	<ul style="list-style-type: none"> • Binding to specific protein on surface of tumor or immune cell • Checkpoint blockades inhibit immune suppression • Other mAbs can mark cells for death or aid in immune activation 	Immune cells, cancer cells
Small Molecules	<ul style="list-style-type: none"> • Extra and Intracellular targets, must diffuse or transport through cell membrane • Cytotoxins → Cause damage to various cell functions • Targeted drugs → disruption of specific pathways critical for tumor cell progression 	Cancer cells, rapidly dividing cells

3. Intratumoral transport

In addition to the mechanism of action for the active component, the design of IT therapy formulation requires an understanding of molecular transport within the TME after the drug/formulation is delivered. After delivery (injection) into the tumor, the drug/formulation will undergo several transport and kinetic processes (**Figure 2**) that will ultimately determine retention or elimination of the anti-cancer therapy (**Table 2**). Major molecular transport and kinetic processes within the TME include extracellular binding, cellular uptake and intracellular binding, and finally exfiltration from the TME.

Molecular transport through normal extracellular matrix is based on both diffusion along a concentration gradient as well as advective convection (or bulk transport of mass) along a pressure gradient.¹⁹ However, since elevated IFP makes the bulk transport (i.e. convection) of the IT therapy negligible in the TME, transport of anti-cancer agents after IT administration are typically governed by diffusion.^{9, 20} Though the blood vessels represent an escape route for the therapeutic agent, the abnormal and poorly organized vasculature of the TME increases retention at the tumor cells that are distant from the vessels.²¹ The absence of functional lymphatics in the TME reduces the elimination of the agent, improving IT retention.²²⁻²³ Despite the relatively ineffective lymphatic drainage in the TME, peritumoral lymphatics are a major route for metastasis and the local loss of IT therapeutics.²⁴ Angiogenesis, which seeks to normalize tumor vasculature leading to increased blood flow and reduced IFP, can result in decreased retention time.²⁵⁻²⁷ Vascular permeability can also decrease tumor retention time for small molecules, but this characteristic is purported to be insignificant for macromolecules.²⁸⁻²⁹

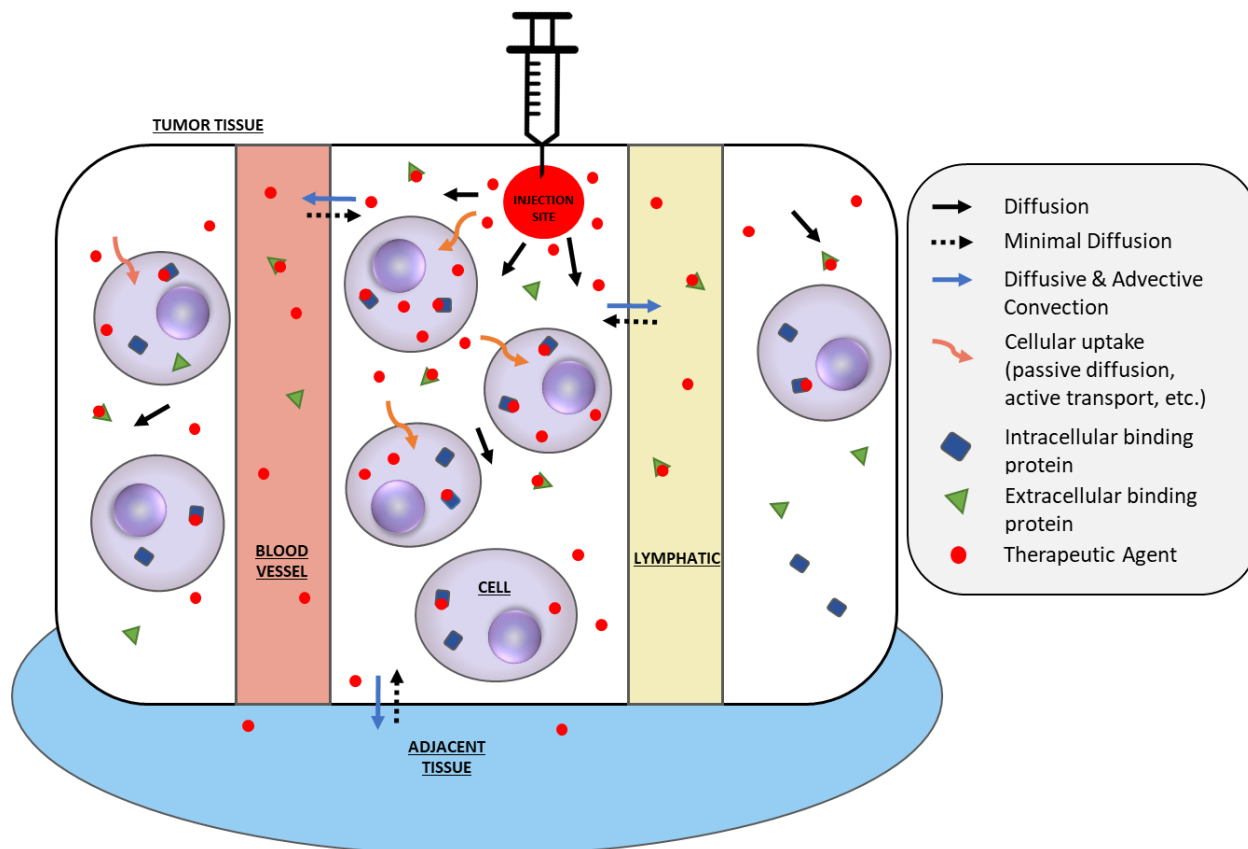


Figure 2. Representative transport and kinetic processes in intratumoral injection therapies. The therapeutic agent can diffuse through the TME, enter the cell, be bound by extracellular or intracellular proteins, unbind, or leave the tumor into blood vessels, lymphatics, peripheral blood, or adjacent tissue by diffusion and advective convection. Diffusional transport of the agent back into the tumor is expected to be minimal.

Densely packed collagen fibers are characteristic of the TME and pose transport resistance, which likely results in an overall increase in retention of IT therapy, although dense collagen may also restrict access to sites within the tumor.^{19, 30} Fibrillar collagen and high IFP contribute to a high mechanical stress in the tumor,³¹ which promotes diffusion over convection for the IT therapy. Cellular packing density can also affect drug diffusion; loosely packed tumor cells can positively impact retention at tumor by enabling fast and thorough penetration of the therapeutic agent.³² Regions of tightly packed cells, on the other hand, impair the penetration of the therapeutic

agent throughout the tumor. Finally, cellular uptake or binding of the therapy can occur by passive diffusion, active uptake, or other mechanisms depending on molecular properties.

Drug features such as molecular size, charge, and other properties influence intratumoral residence time. Water soluble small molecules diffuse more easily in the TME resulting in a lower retention in the tumor,³³ but increases in molecular hydrodynamic radius can reverse this effect. It is critical to balance molecular size such that a therapeutic or its carrier is small enough to diffuse through the TME while avoiding clearance through lymphatic drainage or cellular uptake.³⁴ Large molecules such as monoclonal antibodies, for instance, can have limited tumor retention due to endocytic clearance after IT administration.³⁵ Drug diffusion and retention deep inside the tumor mass is affected by binding kinetics and affinity.³⁶ Molecular charge may also be exploited such that the acidic extracellular pH in the tumor has a positive impact on retention. The lymphatics are a primary mechanism for clearance of subcutaneously injected mAbs, and the clearance rate is mainly dependent on the isoelectric point (pI).³⁷ Hence, careful antibody design utilizing physiologically based pharmacokinetic models in the development stage could lead to new generations of antibody-based therapies with enhanced local tissue and IT retention. The many factors that influence TME transport offer unique opportunities for the retention of drugs injected intratumorally such that the exploitation of these abnormalities can be harnessed to maximize therapeutic effects. Moreover, these complexities of IT transport could be modeled *in vitro* using biomaterials to create a platform where the IT retention can be predicted for these therapies before moving to clinical trials. The technology described in Chapter 2 attempts to model some features of IT transport *in vitro* to better study the retention of therapies.

Table 2. Factors affecting transport of therapy out of the tumor after intratumoral injection.

Tumor tissue factors	Phenomena
<i>Microvascular permeability</i>	Decreases retention at tumor, but insignificant where blood vessel fenestration is present
<i>Abnormal vascular architecture</i>	Increases retention at the tumor
<i>Absence of lymphatics</i>	Increases retention at the tumor
<i>Interstitial fluid pressure (IFP)</i>	Increased IFP increases retention time at the tumor but decreases it close to vessels
<i>Solid stress elevation</i>	Increases retention within the tumor, but decreases the retention close to vessels
<i>Angiogenesis</i>	Decreases retention at the tumor
Physicochemical factors	Phenomena
<i>Concentration gradient</i>	Increases diffusion out of tumor, decreasing retention
<i>Water solubility</i>	Water soluble agents diffuse easily in the TME, decreasing retention in tumor
<i>Extracellular pH</i>	Effect on retention at tumor depends on the carcinogenic agent's molecular properties (pI, pKa)
<i>Fibrillar collagen</i>	Increases retention at tumor
<i>Cellular packing density</i>	Low packing density increases retention at tumor

4. Biomaterials for *in vitro* modeling of the tumor microenvironment

Creating an *in vitro* model of the TME to study the complexity of cancer progression mechanisms and metastasis is an active challenge for bioengineers.³⁸ Studying the tumor microenvironment using 3D biomaterial-based models is expected to lead to the development of novel therapeutics more reliably than traditional 2D tissue culture models and may reduce the need for animal models.³⁹ Through 3D cancer cell cultures, a better correlation to human clinical trials in terms of the response to chemotherapeutic agents has been reported,⁴⁰ overcoming the challenges caused by 2D cell culture, which is not representative of the structure of soft tissue.⁴¹⁻⁴² However, the extracellular matrix (ECM) in tumors has been shown to play a key role in cancer progression,⁴³ and the use of biomaterials seeks to account for it in tumor models.⁴⁴ For IT drug delivery, the intratumoral retention time is a key factor, and the existing models do not focus on modeling this *in vitro* to provide useful insight for IT drug screening.

a) Types of biomaterials

Biomaterials can be classified according to their polymer's origin,⁴⁵ and there are three types that have been used to attempt to emulate the TME faithfully: naturally derived, synthetic, and semi-synthetic biomaterials. While naturally derived biomaterials (Matrigel, decellularized ECM,

collagen, fibrin, alginate, silk) are ideal for replicating cell-matrix interactions, they have batch-to-batch variability and the resulting scaffolds have limited mechanical stiffness, porosity, and number of cell adhesion sites. Synthetic biomaterials (PLG, PLA, PLGA, PEG) have superior structural complexity to isolate specific microenvironmental cues and tunable material properties, but their fabrication methods may be cytotoxic and have limited bioactivity. Finally, semi-synthetic biomaterials (hyaluronic acid, chitosan-PCL, peptides-based hydrogels) have the capability to achieve the bioactivity of natural materials while keeping a wider range of tunability in the structural complexity and material properties, but their fabrication methods may be cytotoxic and the bioactivity of their natural components could be compromised.⁴⁶ The technology developed in Chapter 2 combined the three types into the scaffolds by implementing collagen type I (naturally-derived), PEG (synthetic) and, as the main component, hyaluronic acid (semi-synthetic).

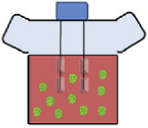
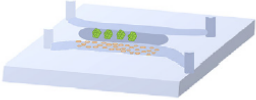
b) Types of in vitro tumor models

*Brancato et al.*³⁹ offer a comprehensive review of the various types of 3D models of cancer that can be used for drug screening, which is the process of testing and optimizing compounds from libraries. In general, categories include scaffold-free systems, scaffold-based or hydrogel-based systems, bioreactors, microcarriers and tumor-on-chip. **Table 3** summarizes their respective advantages and pitfalls.

Scaffold-free systems are mostly spheroids in hanging-drop 3D culture, with InSphero AG (Switzerland) being a pioneering company in this area,⁴⁷ or organoids (*in vitro* aggregates, derived from stem cells, capable of self-organization, recapitulating some tumor functionality)⁴⁸⁻⁴⁹ without using exogenous matrices. Scaffold-based tumor models are the type studied in this thesis, and Chapter 2 designs one specifically tailored to IT drug screening. While the incorporation of cells

was not heavily studied, biocompatibility is reported in Chapter 3 and future directions are detailed. Bioreactors, microcarriers and tumor-on-chip models escape the scope of this thesis.

Table 3. Types of 3D cancer models for drug screening. Reprinted from *Brancato et al.*³⁹, with permission from Elsevier.

3D Tumor Model	Graphical representation	Advantages	Pitfalls
Scaffold-free systems		<ul style="list-style-type: none"> • Co-cultures possible • Optically transparent • HTS approach possible 	<ul style="list-style-type: none"> • No support or porosity • Poor control over spheroids/organoids size • No cell/ECM interactions
Scaffold-based system		<ul style="list-style-type: none"> • Co-cultures possible • Large variety of materials, also decellularized matrix • Customizable • Affordable cost • Off-the-shelf scaffolds 	<ul style="list-style-type: none"> • Possible scaffold-to-scaffold variation • Not always optical transparent • Cell removal may be difficult • HTS options limited
Hydrogels		<ul style="list-style-type: none"> • High similarity to the <i>in vivo</i> conditions • Promotion of cellular attachment, proliferation, and differentiation • HTS approach sustainable 	<ul style="list-style-type: none"> • Gelling mechanisms • Batch to batch variation • Undefined constituents in natural gels • Not always optical transparent • Poor mechanical properties
Bioreactors		<ul style="list-style-type: none"> • High similarity to the <i>in vivo</i> conditions • High volume cell production • Customizable and controlled culture parameters 	<ul style="list-style-type: none"> • Space required for dynamic cell culture • High costs for dynamic cultures • HTS options laborious
Microcarriers		<ul style="list-style-type: none"> • Co-cultures possible • High similarity to the <i>in vivo</i> conditions • Customizable • HTS approach sustainable 	<ul style="list-style-type: none"> • Limited control over microtissues size • Not biodegradable microcarriers
Tumor-on-chip		<ul style="list-style-type: none"> • <i>In vitro</i> organ specific systems • High gas permeability • Transparent • Commercial availability 	<ul style="list-style-type: none"> • Required expertise • High cost for the microfabrication • HTS options limited

c) Hyaluronic acid-based scaffold tumor models for drug screening

Hyaluronic acid (HA) is a negatively-charged polysaccharide of high molecular weight found as a major component in both normal tissue and tumor ECM.⁵⁰⁻⁵¹ In tissue engineering, it is commonly used after modifying the HA chains with methacrylate to fabricate scaffolds with tunable properties and that can be functionalized to increase cell adhesion.⁴⁶ A few existing HA-based scaffold tumor models with drug screening applications are described here.

*Fong et al.*⁵² created a scaffold tumor model by culturing bone metastatic patient-derived prostate cancer cells in an HA-based hydrogel to study tumor cell morphology, viability and phenotype, and treated these models with docetaxel to test the drug's anticancer effects by observing differences in the proportion of apoptotic cells. *Xu et al.*⁵³ created a bilayer HA-based scaffold loaded with heparin-binding EGF-like growth factor loaded in microparticles in the top layer and prostate cancer cells in the bottom layer. This bilayer model offered a different approach for screening of growth factors but still did not model IT delivery and transport. *Ananthanarayanan et al.*⁵⁴ designed an interesting brain-mimetic HA-based tumor model with tunable stiffness, modified to culture glioblastoma cells. Although they did not have a drug screening application, they had interesting findings regarding glioma cell behavior as a function of scaffold stiffness, which, as explained later, is hypothesized to be a key factor for IT delivery.

Covering the scaffold with varying concentrations of an anticancer drug may serve as a model of conventional intravenous administration (transport into a tumor) but is not representative of intratumoral delivery. The existing HA-based scaffold models measure anticancer efficacy of drugs by observing apoptosis in 3D-cultured cells, which is determined by how much drug diffuses into the scaffold. For IT delivery, however, efficacy is impacted by how slowly the drug diffuses out of the tumor. The technology designed in Chapter 2 is, to the best of our knowledge, the first work to explore hydrogels as scaffold-based tumor models for IT drug screening.

d) Modeling the tumor's biomechanical properties

Tumor cells have the ability to remodel the ECM and alter its mechanical properties, and this altered matrix influences tumor progression.⁴³ ECM rigidity has been shown to direct pathological processes involving cell locomotion,⁵⁵ such as metastasis, and because tumors are

stiffer than normal tissue, the increased matrix stiffness of the TME has been shown to affect cytoskeletal tension resulting in altered tissue phenotype.⁵⁶

Collagen, the most abundant ECM scaffolding protein in the stroma, is a significant contributor to tissue stiffness and collagen fibers play a dominant role in maintaining the structural integrity of tissues and organs.⁵⁷ In cancer, however, collagen metabolism is deregulated and tumor progression has been accompanied by increased collagen expression, elevated deposition, altered organization and elevated matrix metalloproteinase activity.⁵⁸ Increased expression of type I collagen is associated with elevated incidence of metastasis,⁵⁹ and high collagen I concentrations are characteristic of high mammographic density associated with increased breast cancer risk.⁶⁰ Collagen crosslinking, the oxidative covalent process initiated by lysyl oxidase (LOX),⁶¹ is elevated in tumors⁶² and the excessive accumulation of collagen is a hallmark of fibrosis,⁶³ which also increases risk of malignancy and is linked to poor patient prognosis.⁶⁴ Cancer patients with fibrotic “stiff” regions are well known to have a poor prognosis,⁶⁵ and the relationship between collagen crosslinking, tissue fibrosis and stiffness in cancer has become more evident. Thus, fibrotic regions are hypothesized to play a significant role in IT delivery too.

High matrix stiffness and collagen concentration or crosslinking was shown to induce a malignant phenotype in normal mammary epithelium using 3D *in vitro* models consisting of RGD (arginine-glycine-aspartic acid)-derivatized polyacrylamide hydrogels,⁵⁶ demonstrating that elevated matrix stiffness in tumors has many implications in cancer progression. However, the implications of fibrotic regions and elevated stiffness of tumors in IT delivery have not been explored using any existing *in vitro* tumor model. Through shear rheology of mammary glands at normal, premalignant and invasive cancer stages, it has been shown that tumors are much stiffer (900-1200 Pa average elastic modulus, G') than premalignant (~200 Pa average G') or normal

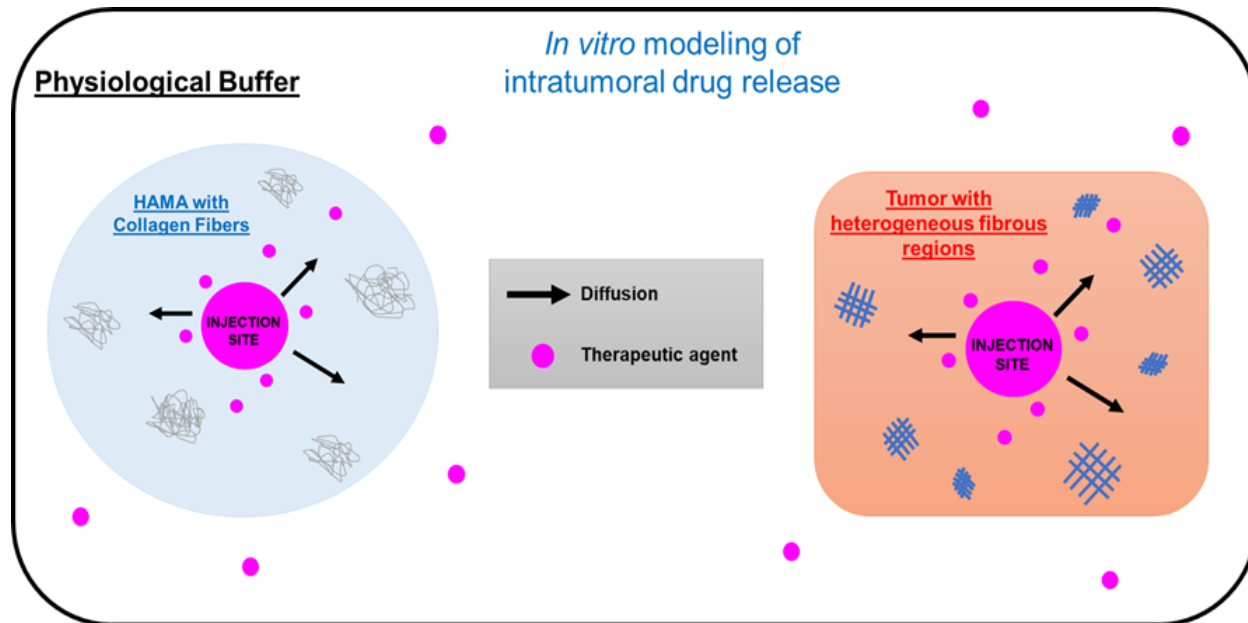
(~100 Pa average G') mammary tissue.⁶⁶ Therefore, we hypothesize that modeling the tumor's bulk biomechanical properties could be achieved by matching its elastic modulus with that of scaffolds, and the influence of fibrotic regions in the tumor can be modeled by adding highly concentrated type I collagen fibers dispersed throughout HA-based scaffolds.

5. Remarks for this thesis

In order to expedite the screening of IT therapies, an *in vitro* tumor model for assessing therapeutic advantages such as prolonged tumor retention is needed. However, none of the existing 3D tumor models can properly study retention of IT therapies and transport from the site of administration. Thus, this thesis presents an innovative tumor tissue-mimicking biomaterial designed to simulate IT injection and model IT retention and transport using *in vitro* drug release studies. The scaffold is based on HA, and the influence of fibrotic regions in the tumor is studied via concentrated collagen I fibers added to the model. The stiffness of tumor tissue is also studied, and the scaffolds are engineered to attempt to match the tumor stiffness while evaluating the transport of compounds.

Chapter 2: Constructing a tumor tissue-mimicking biomaterial to study intratumoral drug transport

As prepared for peer-reviewed submission.



1. Introduction

Due to the complexity of cancer and the need of better therapeutics, constructing an *in vitro* model of the tumor microenvironment (TME) has become an appealing task to study mechanisms related to cancer progression and metastasis.³⁸ There has been a plethora of biomaterials used to design tumor models *in vitro*, which exceeded the performance of 2D cell culture and even animal models in some instances.^{44, 46, 67-68} Hence, the application of tumor models for drug screening and optimization has become very promising.³⁹ Various tumor models in scaffold format⁵²⁻⁵⁴ as well as others using microfluidics and cancer-on-a-chip technology⁶⁹⁻⁷¹ have been used to test anticancer therapeutics. However, there is no tumor model designed to screen intratumoral (IT) therapies, where the considerations are different than those of chemotherapeutics administered systemically.

IT delivery consists of injecting a drug or formulation directly into the tumor, which bypasses physiological obstacles encountered during systemic circulations and tumor penetration and, thus, reduces immune-related adverse effects that are present in the systemic delivery of cancer therapeutics.¹⁻³ IT retention is a key factor in the design of these localized interventions, so the biophysics of the TME and IT transport play a pivotal role. In normal extracellular matrix (ECM), molecular transport is driven by diffusion along a concentration gradient and convection, or bulk transport, along a pressure gradient.¹⁹ The elevated interstitial fluid pressure characteristic of tumors, however, makes the convective bulk transport negligible, making diffusion the governing transport force.^{9, 20} Thus, a model to screen IT delivery needs to be diffusion-driven. Furthermore, ECM rigidity has been shown to control and promote pathological processes involving cell locomotion,⁵⁵ such as metastasis, and because tumors are stiffer than normal tissue, the increased matrix stiffness of the TME has been shown to affect cytoskeletal tension resulting in altered tissue phenotype.⁵⁶ Biomaterials' matrix stiffness has also been shown to influence the phenotype and epigenetics of 3D-cultured cancer cells.⁷² Therefore, matrix stiffness is an important consideration for a model to screen IT delivery.

Hyaluronic acid (HA), a negatively-charged polysaccharide of high molecular weight found as a major component in both normal tissue and tumor ECM,⁵⁰⁻⁵¹ was used as the base polymer of the tumor tissue-mimicking hydrogel model in this study. The HA chains were modified with methacrylate (HAMA) to crosslink it, which is widely used in tissue engineering.⁴⁶ Collagen, the most abundant ECM scaffolding protein in the stroma, is a significant contributor to tissue stiffness and collagen fibers play a dominant role in maintaining the structural integrity of tissues and organs.⁵⁷ Collagen crosslinking is elevated in tumors⁶² and the excessive accumulation

of collagen, particularly type I collagen, is a hallmark of fibrosis.⁶³ Thus, type I collagen fibers (Col) were incorporated in the scaffolds to model tumor fibrosis.

In this study, tumor-tissue mimicking scaffolds were specifically designed to study IT delivery. The bulk biophysical properties of head and neck (HN) tumors from mice were studied through stiffness measurements by shear rheology, and the stiffness of HA hydrogels was tuned using collagen I fibers to emulate that of the tumors. Next, implementation of hydrogels as IT injection site simulators was explored. In order to test the scaffold's ability to model intratumoral diffusional transport *in vitro*, two compounds were tested: glatiramer acetate (GA) and polyethylene glycol (PEG). GA was previously observed to precipitate and electrostatically bind to ECM when injected subcutaneously.⁷³ Thus, if injected intratumorally, GA was expected to interact electrostatically with the HA in the TME and, consequently, have a longer IT retention than a neutrally charged molecule like PEG. IT transport was studied by dispersing these compounds or injecting them into HA hydrogels. GA and PEG were also injected in resected murine head and neck tumors and transport was studied for comparison.

2. Materials and methods

a) Materials

Triethylamine, glycidyl methacrylate and tetrabutylammonium bromide used in the methacrylation of 1MDa hyaluronic acid, as well as the gelatin type A from porcine skin, methacrylic anhydride, and Irgacure 2959 were purchased from Sigma Aldrich (St. Charles, MO). Lyophilized fibrous type I bovine collagen was obtained from Advanced BioMatrix (San Diego, CA). Polyethylene glycol diacrylate (PEGDA) 10,000 kDa was purchased from SunBio (Gyeonggi-do, Korea). Glatiramer acetate in the form of Copaxone[®] 1 mL pre-filled syringes from Teva Neuroscience, Inc. (Kansas City, MO) were kindly donated by Dr. Sharon Lynch at the

University of Kansas Medical Center. Polyethylene glycol ~5,000 kDa was bought from Creative PEGworks, Rhodamine B (Rho) NHS Ester was synthesized in the lab as detailed below, and Sulfo-Cyanine7 (Cy7) NHS Ester was bought from Lumiprobe Life Science Solutions. Physiological buffer was made by dissolving 12.8 g NaCl, 0.18 g MgCl₂ hexahydrate, 0.8 g KCl, 0.4 g NaN₃, 0.4 g CaCl₂ dihydrate and 4.2 g of NaHCO₃ in 2 L of doubled distilled water by stirring, and the pH was adjusted to 7.4 by sparging CO₂ gas into the solution.

b) Methacrylation of hyaluronic acid

Methacrylated HA (HAMA) was made by first solubilizing 2 g of 1MDa HA overnight in 100 mL of ultrapure water and 100mL of acetone. 4.4 mL of tetrabutylammonium was added to 4.4 mL of glycidyl methacrylate and 4.4 mL of triethylamine, vortexed, and then added slowly into the solubilized HA. After carrying out the reaction for 24 hours while stirring, 200 mL of ultrapure water was added and stirred for 10 minutes. The solution was transferred into molecular porous membrane tubing (MWCO 12-14,000, Fisher Scientific, MO) and dialysis was carried out for 5 days to get rid of any unreacted reagents. After dialysis, the solution was frozen and freeze-dried for 2 days to obtain lyophilized HAMA.

c) Fluorescent dye-labelling of GA and PEG

GA and PEG were fluorescently labeled with rhodamine B for release studies in the hydrogel models. Synthesis of Rhodamine B NHS Ester and the following procedure was adapted from Meng *et al.*⁷⁴ Copaxone[®] dialyzed in water (7 μmol, 7000 Da was used as the MW of GA for calculation) was reacted with 2 equivalents (14 μmol) of N-(6-(diethylamino)-9-(2-(((2,5-dioxopyrrolidin-1-yl)oxy)carbonyl)phenyl)-3H-xanthen-3-ylidene)-N-ethylethanaminium (Rhodamine B NHS Ester) in 10 mM citrate/20 mM phosphate/40 mM borate buffer at pH 7.5 with 20 % DMSO. The reaction was performed at room temperature for 4 hours protected from

light with gentle agitation. To separate labeled drug from excess dye, the reaction mixture was placed into dialysis cassettes with 2 kDa MWCO and dialyzed against 5% DMF in water at pH 2, followed by 0.5 M LiCl solution, and finally water. Dialysis was performed sequentially in each buffer for 24 hours with one buffer change in between for a total of 72 h. The resulting reaction solution was characterized by HPLC for the elimination of the starting materials and lyophilized. For release studies in tumors, 5 equivalents (7000 Da used as MW of GA, 5000 Da was used as MW of PEG) of GA/PEG were reacted with 1 equivalent sulfo-cyanine 7 NHS Ester in 50 mM HEPES buffer pH 7.5 with 20% DMSO. The reaction was performed at room temperature for 4 hours protected from light with stirring. To separate labeled drug from excess dye, the reaction mixture was placed into dialysis cassettes with 2 kDa MWCO and dialyzed in water with buffer change every 12 hours for 72 hours. To ensure the labeled compounds were free of all unreacted dye after their respective reactions, the fluorescently labeled GA and PEG were analyzed through HPLC conducted on a Waters Alliance HPLC system equipped with a dual wavelength UV-vis detector. GA-Cy7 and PEG-Cy7 were characterized using Waters XBridge BEH C₁₈, 5 μ m, 4.6 \times 250 mm, linear gradient from 5 to 95% acetonitrile (+0.05% TFA) in water (+0.05% TFA) over 30 min, detection at 214 nm. Similarly, GA-Rho and PEG-Rho were characterized using Waters XBridge BEH C₄, 3.5 μ m, 4.6 \times 150 mm, linear gradient from 5 to 95% acetonitrile (+0.05% TFA) in water (+0.05% TFA) over 30 min, detection at 369 nm.

d) Fabrication and imaging of hydrogel scaffolds

Hydrogels with 3% HAMA were prepared by weighing the 3 wt% HAMA and 0.1 wt% Irgacure 2959 photocrosslinker and solubilizing it in 1X phosphate-buffered saline (PBS). Due to the size of the HAMA and the viscosity of the solution, the mixture was manually stirred with a spatula and centrifuged multiple times (~4) until fully solubilized or left in an automatic rotator

overnight. For the models with collagen fibers, pieces of lyophilized concentrated collagen type I fibers were weighed first (1 or 2 wt%), then the HAMA and photocrosslinker were weighed, and the PBS was added last. When PEGDA was part of the models, the 3 wt% PEGDA was weighed first, followed by the photocrosslinker, then PBS and vortexed to solubilize. The collagen fibers were weighed separately and added to the solution, followed by the HAMA. All solutions were then transferred to the well-plate, which was then centrifuged at 1500 min^{-1} for 2 min, injected with the drugs in the case of the reservoir models, and cured at 365 nm for 7 min in a UVP Transilluminator (Analytik Jena AG, Germany).

In order to observe the porosity of the HAMA gels and the incorporation of the collagen type I fibers, scanning electron microscopy (SEM) was performed at 60X, 100X and 200X on dehydrated 3% HAMA and 3% HAMA 1% Col hydrogels using a FEI Technai F20 XT Field Emission Transmission Electron Microscope. Swelling ratios of 3% HAMA and 3% HAMA 1% Col hydrogels were obtained by lyophilizing triplicates of these groups, measuring their initial dry mass (M_d) and the wet mass of the hydrogel at swelling equilibrium after 2 days (M_w), and calculating the swelling ratio = $(M_w - M_d)/M_d$.⁷⁵ Fluorescent imaging of the gels was done in a 12-well plate covered with black electrical tape, using a MaestroFlex whole body imager (Cambridge Research and Instrumentation, MA) employing an excitation filter of 575–605 nm and a long-pass emission filter of 645 nm. The reservoir 3% HAMA gels were prepared as detailed below, placed at the bottom of the well with the injection site facing up, and covered in the physiological buffer. A 5 μL drop of GA-Rho at the same concentration injected was placed on an adjacent well before taking the image at each timepoint to auto-adjust the brightness of the imager consistently to that drop as a reference.

e) Staining of tumor tissue and biomaterial

Resected tumors and 3% HAMA and 3% HAMA 1% Col hydrogels were cryo-embedded with Tissue-Plus O.C.T. Compound (Fisher Scientific, MO) and sectioned into 20 μm on microscope slides in triplicate. Slides were then fixed in 10% neutral buffered formalin for 10 min, and either Masson's Trichrome Stain or Aniline Blue Stain (Sigma Aldrich, MO) was applied. Images of the stained tissues were obtained using the EVOS[®] FL Auto Imaging System from ThermoFisher Scientific.

f) Rheological analysis

Optimal viscosity for simulation of tissue injection *in vitro* was determined by that of un-crosslinked 3% 1MDa HAMA, which was measured using the microVISC viscometer (RheoSense, CA). Rheological testing of the various hydrogel scaffolds and tumor tissue was carried out across oscillatory frequency and strain sweeps using an AR2000 rheometer (TA Instruments, DE). Hydrogels were tested as produced on a 24-well plate after being allowed to soak on PBS overnight to reach swelling equilibrium, while tumors were cut into cylindrical cross-sections using a disposable 10 mm biopsy punch and a disposable scalpel to ensure the top and bottom were flat right after being resected from the mice to ensure that the tissue was fresh. Elastic modulus (G') and loss modulus (G'') were recorded. Strain sweeps consisting of oscillatory measurements at a low fixed frequency of 1 Hz with increasing strain amplitudes were used to determine the strain percentages corresponding to the gels' and the tumors' viscoelastic regions that could be used for frequency sweeps. Frequency sweeps consisted of oscillatory measurements at a low fixed strain of 1% with increasing frequency amplitudes from 0.01 Hz to 10 Hz, which were run to determine the G' and G'' of the constructs as a function of frequency.

g) *In vitro* drug release

For the dispersed hydrogel models, 25 μL of 20 mg/mL GA-Rho or PEG-Rho solubilized in 40 mg/mL mannitol was added into the gel solution, mixed homogeneously and UV-cured (**Figure 3**). After curing, the scaffolds were transferred to a 50mL Falcon tube containing 8 mL of physiological buffer. A set of positive controls was prepared and UV-radiated in the same way but without a crosslinker, so that the fluorescently labeled drug in the controls underwent the same processing conditions as the samples but would fully solubilize into the buffer to serve as a 100% release control.

To ensure uniform injection into the wells at half the depth of the gel in the reservoir models, a 3D-printed injector was designed and customized for standard 0.5mL insulin syringes (BD Veo, NY) and 24-well plates. Reservoir hydrogel models were made utilizing the 3D-printed injector and insulin syringes to inject 10 μL of 20 mg/mL GA-Rho or PEG-Rho solubilized in 40 mg/mL mannitol into the center of the gel (**Figure 5a**), UV-cured and transferred to a 50mL Falcon tube containing 8 mL of physiological buffer. Positive controls were injected similarly for the reservoir models and underwent the same curing conditions without the crosslinker, then were fully solubilized in the physiological buffer to serve as 100% possible release control. One mL of the buffer was collected at the timepoints 0, 1, 2, 3, 6, 12, 24, 48 and 72 h, and 1 mL of fresh physiological buffer was added to replace the amount withdrawn. At the end of the release studies, the 270 μL of each timepoint was plated in a black flat-bottom 96-well plate in duplicates, and the fluorescence was measured using a Synergy HTX multi-mode plate reader (BioTek T4) at 585 nm emission, 555 nm excitation and 105 gain. The concentration at each time point was determined by dividing the fluorescence at the timepoint by the fluorescence of the 100% controls and

multiplied. Fluorescence values were adjusted to account for GA or PEG that was taken out during sampling and then converted to percentage of GA or PEG released as a function of time.

h) Mathematical modeling of diffusion coefficients

Release data from the various dispersed and reservoir models were fit using Fick's second law of diffusion (eqn. 1):

$$\frac{\partial c}{\partial x} = D \left(\frac{\partial^2 c}{\partial x^2} + \frac{\partial^2 c}{\partial y^2} + \frac{\partial^2 c}{\partial z^2} \right) \quad (1)$$

Reservoir models were mathematically modeled as a cylindrical reservoir device with non-constant activity source, given that the initial concentrations do not exceed the drug solubility. Drug diffusion is the rate limiting step considered in the mathematical models.⁷⁶

Considering a cylindrical reservoir geometry and perfect sink conditions in the surrounding solution, and assuming one directional radial diffusion, constant partition coefficient of $K=0.2$ and that the drug is homogeneously distributed in the reservoir (injection site), Fick's law of diffusion can be applied to derive the following equation for the amount of drug released at time t relative to the total drug in the scaffold (M_∞):

$$\frac{M_t}{M_\infty} = 1 - \exp \left[- \frac{(R_i H + R_0 H + 2R_i R_0) D K t}{R_i^2 H (R_i - R_0)} \right] \quad (2)$$

where R_i and R_0 are the inner and outer radii of the reservoir and H is the height of the cylindrical scaffold.

Equation 2 was fit to experimental release data for each group using nonlinear least-square regressions with the Microsoft Excel SOLVER add-in program. Effective diffusion coefficients

for each model were calculated by averaging the diffusion coefficients of all the time-points of the release of all three hydrogels in each group, and reported as average \pm standard deviation in cm^2/s .

i) Tumor induction in mouse model

Head and neck tumors were obtained by implanting AT-84 cells, gifted by Aldo Venuti (Regina Elena National Cancer Institute, Rome, Italy), into wildtype C3H mice (Charles River Strain 025, 6-8 weeks old, 20-25g). Both male and female mice were used in the studies. Mice were anesthetized using 5% isoflurane in O_2 for 5 minutes, then one million AT84 cells in 50 μL PBS were injected subcutaneously into the floor of the mouth via an extra-oral route of C3H mice to obtain orthotopic allograft tumors.⁷⁷⁻⁷⁸ Tumors were resected when they reached $\sim 400 \text{ mm}^3$, generally 21-22 days after cell injection, for *ex vivo* release studies, imaging, rheological testing or staining. All mice used for the study were maintained in sterile housing under the veterinary supervision of the University of Kansas Animal Care Unit, which is in compliance with the “Guide for the Care and Use of Laboratory Animals” and is accredited by the Association for the Assessment and Accreditation of Laboratory Animal Care International (AAALAC). The procedure was approved by the Institutional Animal Care and Use Committee.

j) *Ex vivo* intratumoral release and imaging of tumors

Resected tumors were weighed so that the masses of the triplicates injected with GA-Cy7 for *ex vivo* release would closely match the masses of those injected with PEG-Cy7. Tumors were injected with 20 μL of 20 mg/mL GA-Cy7 or PEG-Cy7 solubilized in 40 mg/mL mannitol using insulin syringes. After injection, the tumors were transferred to a 50mL Falcon tube containing 8 mL of physiological buffer. A set of positive controls was prepared by injecting the same amount and concentration on GA-Cy7 or PEG-Cy7 into 8 mL of the buffer to serve as a 100% release control. One mL of the buffer was collected at the timepoints 0, 1, 2, 3, 6, 12, 24, 48 and 72 h, and

1 mL of fresh physiological buffer was added to replace the amount withdrawn. Data were analyzed similarly to the *in vitro* drug release studies adjusting for GA and PEG removed during sampling, with fluorescence measurements done at 782 nm emission, 760 nm excitation and 120 gain.

Fluorescent imaging of the tumors was done in a 6-well plate covered with black electrical tape, using the MaestroFlex whole body imager employing an excitation filter of 710–760 nm and a long-pass emission filter of 800 nm. The resected tumors were glued to the bottom of the well using 3M VetbondTM tissue adhesive, injected with GA-Cy7 and PEG-Cy7, respectively, and covered in the physiological buffer. A 5 μ L drop of GA-Cy7 at the same concentration injected was placed on an adjacent well before taking the image at each timepoint to auto-adjust the brightness of the imager consistently to that drop as a reference (**Figure 8b**). Another set of mice were injected with GA-Cy7 and PEG-Cy7 *in vivo* and sets of three tumors were resected at 2, 4, 24 and 48 h after the injection for fluorescent imaging. Tumors injected *in vivo* were then lined up and imaged under the same conditions as the tumors injected *ex vivo* detailed earlier (**Figure 8c**).

k) Statistical analysis

All statistical analyses were performed using GraphPad Software (GraphPad Software Inc.). Statistical evaluation was performed using one-way analysis of variance (ANOVA) followed by Tukey and Sidak multiple comparison tests for comparisons between three or more groups, and unpaired t-test with Welch's correction for comparisons between two groups only. Statistical significance for all analyses was set at $p < 0.05$.

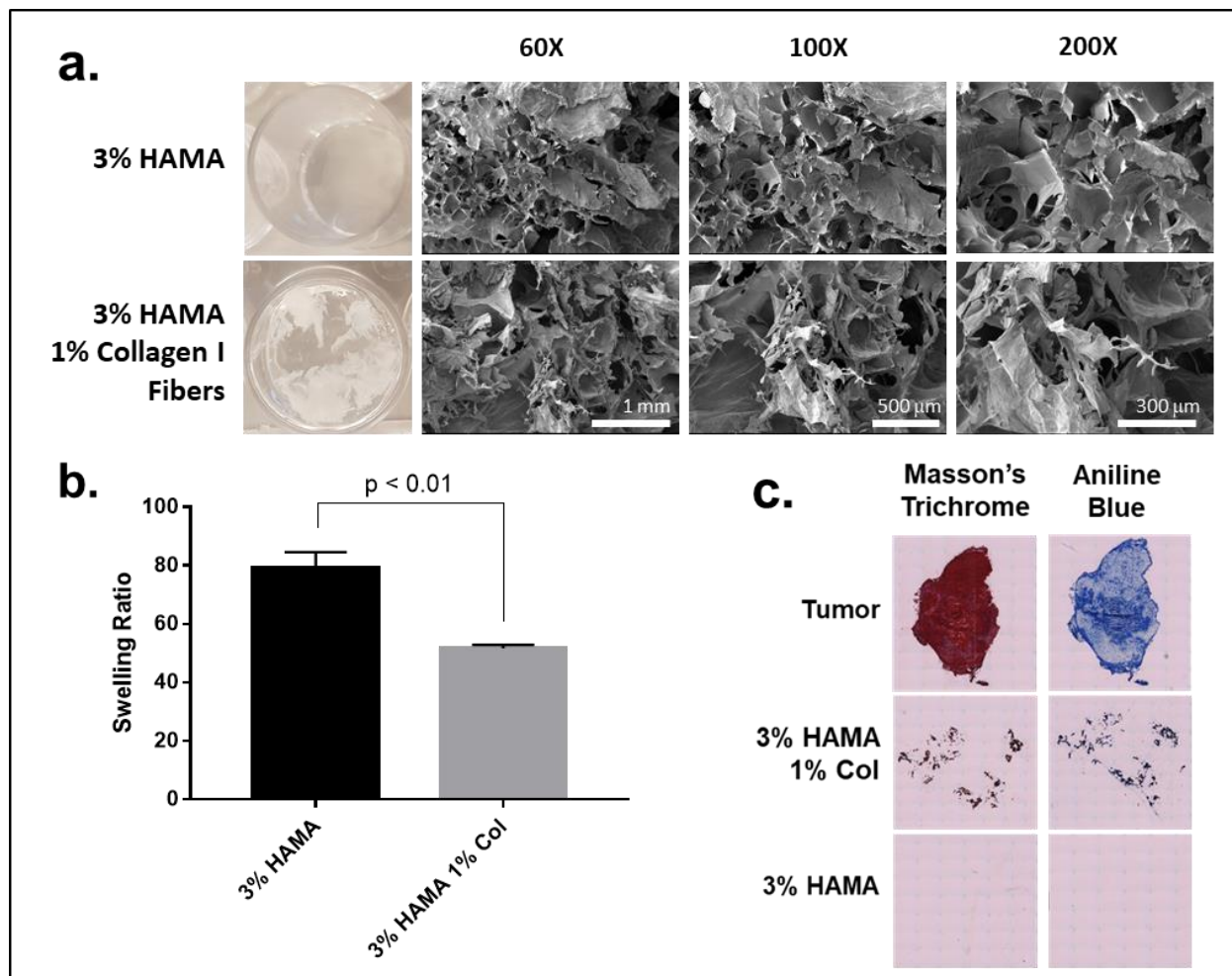


Figure 1. Scaffold characterization. **a)** SEM of 3% HAMA and 3% HAMA 1% collagen type I fibers hydrogels showing their microporous structures and collagen fibers incorporation. **b)** Comparison of swelling ratios of 3% HAMA and 3% HAMA 1% collagen I fibers hydrogels. **c)** Masson's Trichrome and Aniline Blue staining of HN tumor tissue and HAMA-Col scaffolds.

3. Results

a) Synthesis and characterization of hydrogel scaffolds

Hydrogels were designed to serve as tumor models to study the transport and release profile of a therapeutic agent administered intratumorally. To implement this design, the viscosity of the un-crosslinked solution needed to be high enough so the injected therapeutic could be retained at the injection site prior to crosslinking. Methacrylated 1 MDa hyaluronic acid, a polymer available in the normal and tumor extracellular space,⁵⁰⁻⁵¹ provided an adequate viscosity for injection. An

optimized viscosity was attained by using 3% HAMA and was determined to be 13.5 ± 0.7 kPa*s. Fibrous particles of collagen type I were added and dispersed to model the highly variable and heterogeneous fibrotic regions in tumors. PEGDA was also tested in the model, since this neutral, hydrophilic polymer may tune the hydrogel microenvironment.

Porosity of the scaffolds was visualized via SEM, which also showed the physical incorporation of collagen I fibers throughout the HAMA microporous structure (**Figure 1a**). The addition of collagen I fibers (1 wt%) did not impact the overall porosity of the structure, but the swelling ratio was decreased in comparison to that of the 3% HAMA gels (**Figure 1b**). In order to visualize the heterogeneous fibrosis in tumors, histological staining was conducted. Masson's Trichrome, based on three dyes that color collagen as well as other cellular components, was used along with Aniline Blue, which is the dye from Masson's Trichrome that specifically stains for collagen.⁷⁹ Masson's Trichrome stained for more than just collagen in the tumor tissue, so the collagen heterogeneity was not appreciated (**Figure 1c**). Aniline Blue, on the other hand, clearly showed that some regions were more densely stained than others due to the uneven distribution of fibrous collagen in the tumors. In hydrogels, the HAMA matrix was not stained and only the heterogeneously distributed collagen I fibers were stained by both Masson's Trichrome and Aniline Blue.

b) Relative stiffness analysis of scaffolds and solid tumors through shear rheology

Tumor viscoelastic properties were analyzed using a rheometer. The elastic modulus, G' , was used as an indication of the stiffness of the tumors and measured by shear rheology. This measurement assesses how the bulk tumor deforms when shear stress is applied. Various hydrogel models composed of HAMA, PEGDA and collagen I fibers were also analyzed via shear rheology and G' was used to compare stiffness relative to that of the 3 tumors analyzed.

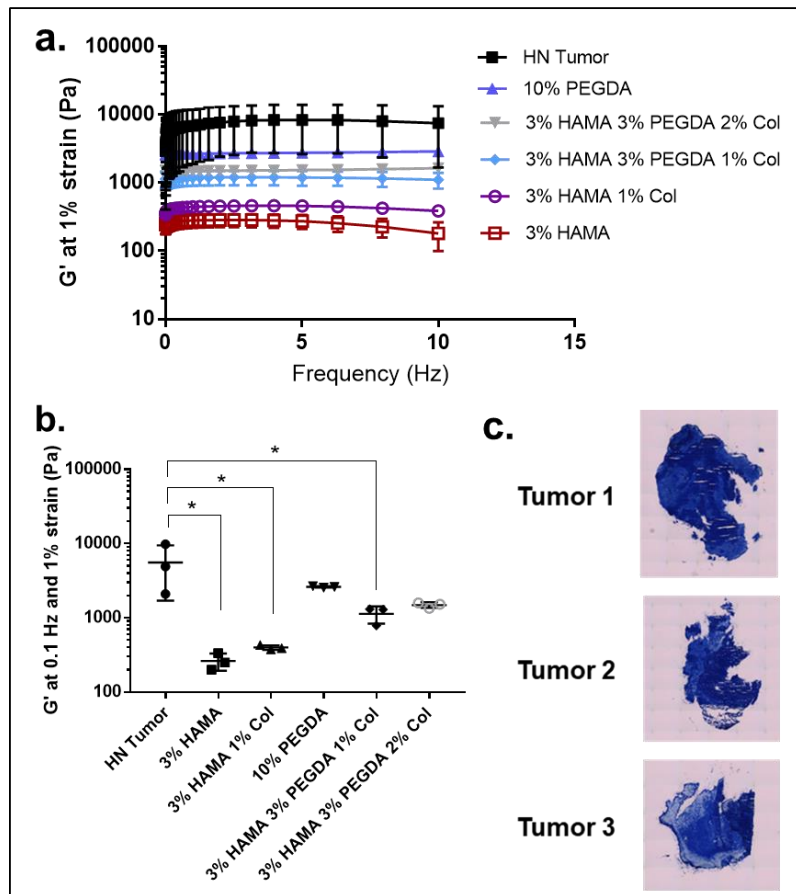


Figure 2. Rheological analysis. **a)** Storage modulus (G') of the tumors and gels of various compositions throughout a frequency sweep (0.01-10 Hz) at 1% strain. **b)** Comparison of relative stiffness between tumor tissue and the gels through the average G' at 0.1 Hz and 1% strain. **c)** Aniline blue histological staining of collagen in the three tumors analyzed, correlating their collagen density to their respective stiffness. (n = 3 replicates per group, * $p < 0.05$)

After verifying the viscoelastic region of the tumors and gels through strain sweeps, an oscillatory frequency sweep was performed at 1% strain to observe the behavior of the tumors' and the gels' G' throughout a wide frequency range (**Figure 2a**). Comparing the G' at a frequency of 0.1 Hz and 1% strain shows the high variability of the tumor's stiffness in comparison to that of the various gels tested (**Figure 2b**). The G' of the 3% HAMA scaffold was the lowest of the gels tested, and that of 10% PEGDA was the highest. Collagen I fibers increased the G' of the HAMA alone, and adding PEGDA increased it even more. Despite the high variability of tumor stiffness, the average G' was found to be significantly higher than that of 3% HAMA, 3% HAMA

1% Col and 3% HAMA 3% PEGDA 1% Col. However, the stiffness was very tunable with collagen I fibers, and the 3% HAMA 3% PEGDA 2% Col scaffold's stiffness matched that of the least stiff tumor and approached the average tumor stiffness.

The heterogeneity of fibrosis was hypothesized to be responsible for the high variability in the G' of the tumors. Thus, Aniline Blue staining was performed on the 3 tumors analyzed, where tumor 1 was the one that presented the highest G' , followed by tumor 2 and the lowest stiffness was that of tumor 3 (**Figure 2c**). Tumor 1 showed the highest collagen density stained blue, followed by tumor 2, which was also dense but showed some less-stained regions. Tumor 3 displayed lightly stained spots related to the least collagen-dense regions observed among the 3 tumors.

c) Scaffolds as *in vitro* models of tumor injection site to study drug release

GA was hypothesized to have a slower release than PEG due to electrostatic interactions with HA or other negatively charged components in the ECM at the injection site in the tumor.⁷³ The release of these compounds was studied *in vitro* using hydrogels as well as *ex vivo* using resected tumors. The two compounds investigated in this study, GA and PEG, were labeled with rhodamine B and studied in a dispersed model to begin to understand the different ways in which they interacted with the different hydrogel matrices. Following this initial assessment, a reservoir model was designed where the release was carried out simulating the injection site of GA and PEG into tissue (**Figure 3**).

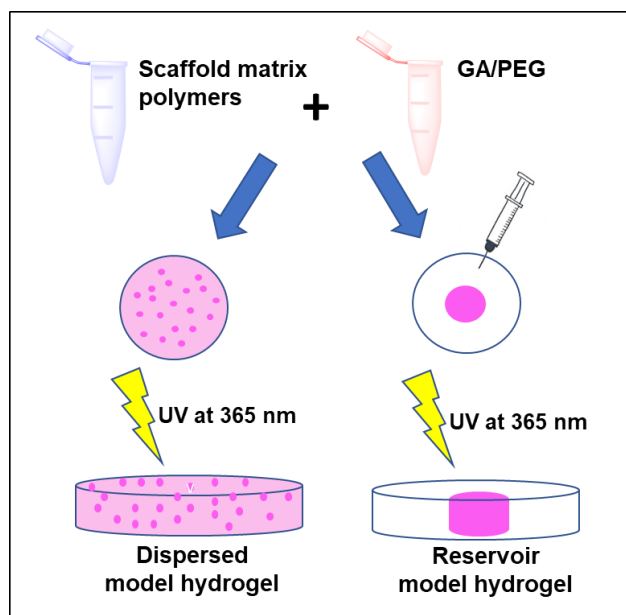


Figure 3. Fabrication of dispersed and reservoir model hydrogel scaffolds.

Dispersed models

To test the hypothesis that GA would have a slower release than PEG, they were first studied in dispersed hydrogel models where the compounds were homogeneously distributed throughout the entire structure of the gel (**Figure 4a**). GA dispersed in 3% HAMA gave a release profile slower than that of PEG dispersed in 3% HAMA, which was significantly faster even after 1 h of release (**Figure 4b and c**). Thus, GA would stay at the injection site longer than PEG if administered intratumorally due to electrostatic interactions between GA and HA. GA was also dispersed in 3% HAMA 1% Col to study the effect of fibers and in 10% PEGDA as a neutral gel. Even after only 1 h, GA was released much faster from the dispersed 10% PEGDA scaffold than the HAMA scaffolds (**Figure 4d**), reaffirming the fact that the release of GA is slowed by electrostatic interactions. The dispersed release of GA in PEGDA was almost identical as the dispersed release of PEG in HAMA, proving that they are both non-electrostatic binding releases. GA dispersed released from 3% HAMA 1% Col was faster than that from 3% HAMA, suggesting

that the collagen fibers used to simulate the heterogeneous fibrosis in tumors hinder electrostatic interactions between GA and HA resulting in a slightly faster release.

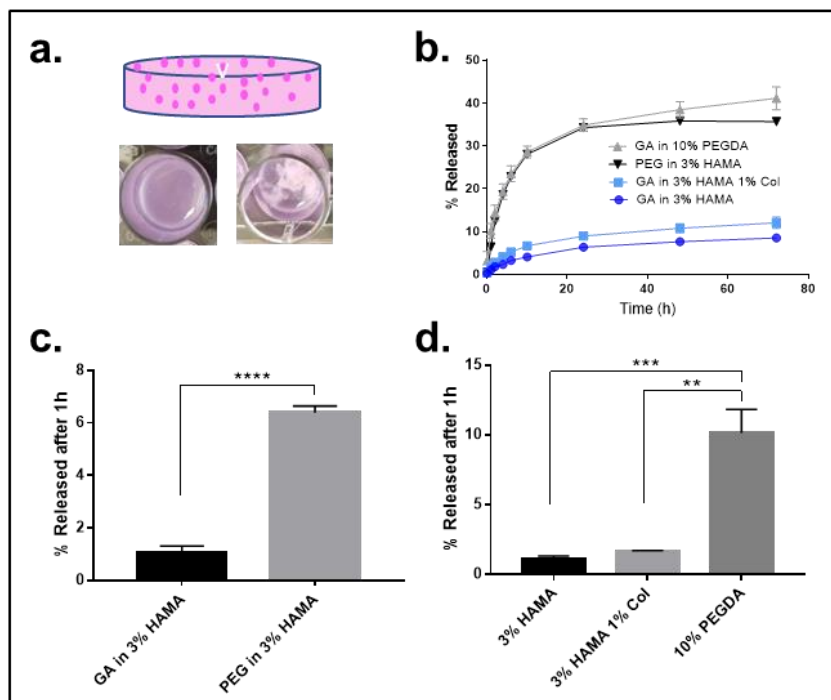


Figure 4. Dispersed model drug release. **a)** 3% HAMA and 3% HAMA 1% Col dispersed models. **b)** GA and PEG release in dispersed models of 3% HAMA, 3% HAMA 1% collagen I fibers, and 10% PEGDA gels. **b)** Comparison of the release rate of PEG and GA in 3% HAMA after 1h. **c)** Comparison of the release rate of GA in the three gels after 1h (n = 3 replicates per group, *p < 0.05, **p < 0.01, ***p < 0.001, ****p < 0.0001).

Reservoir models

Next, intratumoral injection was modeled by injecting GA and PEG in the center of the viscous un-crosslinked hydrogels and then UV-cured (**Figure 5a**). Comparing the release profiles of GA and PEG in 3% HAMA and 3% HAMA 1% Col reservoir models (**Figure 5b**) shows that PEG releases faster than GA, as observed before. Additionally, adding collagen fibers gave a faster release of GA but did not affect the release of PEG, suggesting that fibrotic regions hinder electrostatic interactions of GA with HA resulting in a faster release but, in the case of PEG that does not interact with HA electrostatically, the release remains the same. Addition of PEGDA in 1:1 weight ratio to HAMA made GA release significantly faster, especially at the earlier times

(Figure 5c). Adding collagen fibers to this mix accelerated the release even more. The model with the fastest release was the same model that had a stiffness closest to that of the tumors: 3% HAMA 3% PEGDA 2% Col. PEG showed a significantly faster release than that of GA on the 3% HAMA 3% PEGDA 2% Col reservoir model as early as 24 h and remaining so at 72 h (Figure 5d-e).

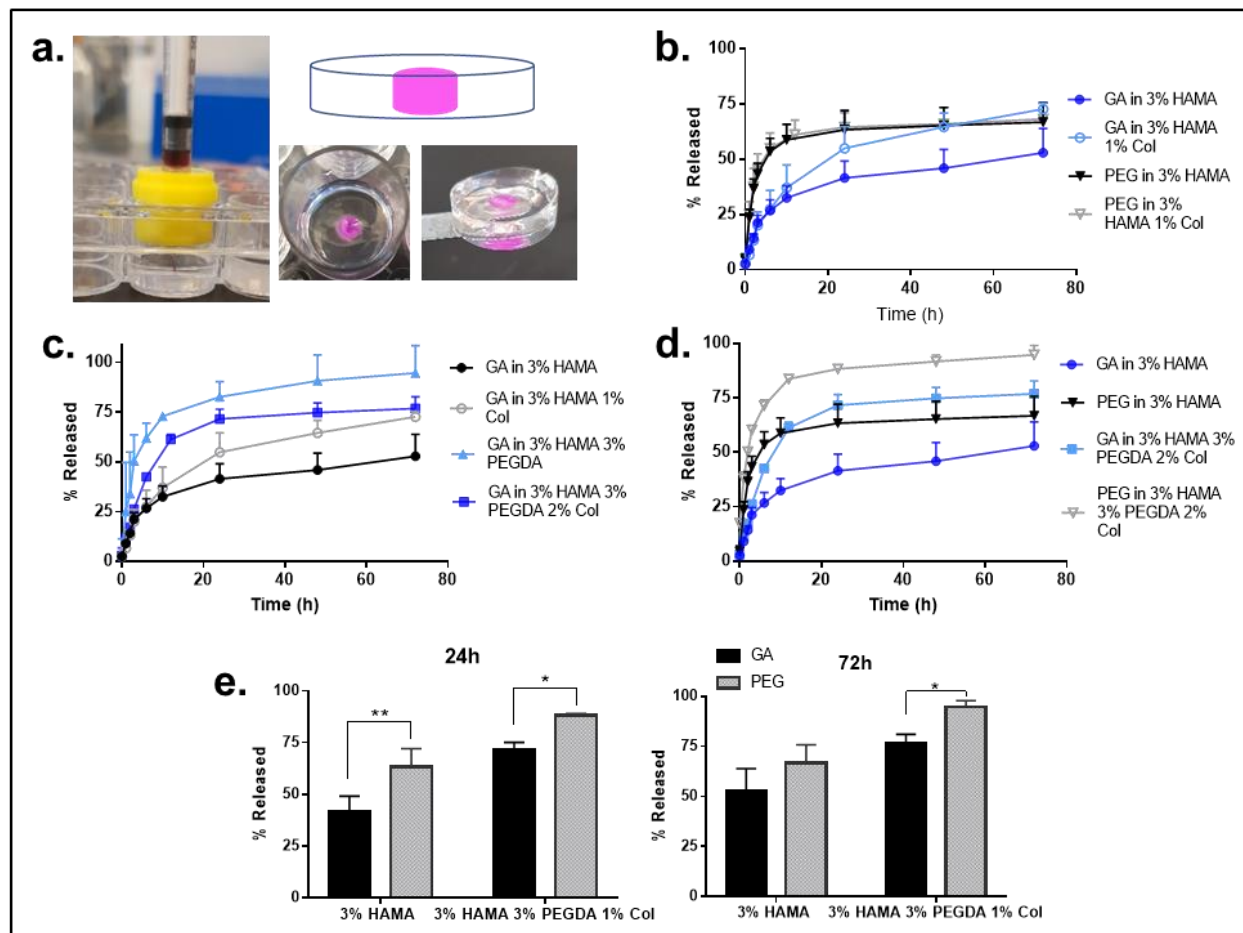


Figure 5. Reservoir model drug release. **a)** Reservoir model injection setup using the 3D-printed injector and an insulin needle. **b)** GA and PEG release in reservoir models of 3% HAMA and 3% HAMA 1% Col gels. **c)** GA release in all the reservoir models studied. **d)** GA and PEG release in reservoir models of 3% HAMA and 3% HAMA 3% PEGDA 2% Col gels. **e)** Comparison of the release rate of PEG and GA in the 2 models analyzed in d after 24h and 72h (n = 3 replicates per group, *p < 0.05, **p < 0.01).

d) Modeling of diffusion coefficients for the *in vitro* release from reservoir models

Diffusion coefficients (D , cm^2/s) were calculated for the release of GA and PEG in the three reservoir models using **Equation 2** (**Table 1**). A cylindrical reservoir model assuming non-constant activity (i.e. finite source) provided an excellent fit to the experimental data of the release profiles using the calculated diffusion coefficients (**Figure 6a**). PEG presented diffusion coefficients (D_{PEG}) significantly higher than those of GA (D_{GA}) in the reservoir models (**Figure 6b**). D_{PEG} was larger than D_{GA} by over a factor of 2 in the 3% HAMA and 3% HAMA 3% PEGDA 2% Col reservoir models, and larger by over a factor of 4 in the 3% HAMA 1% Col model. The larger diffusion coefficients derived from the model support the more rapid diffusion of PEG compared to GA, which is slowed due to electrostatic interactions.

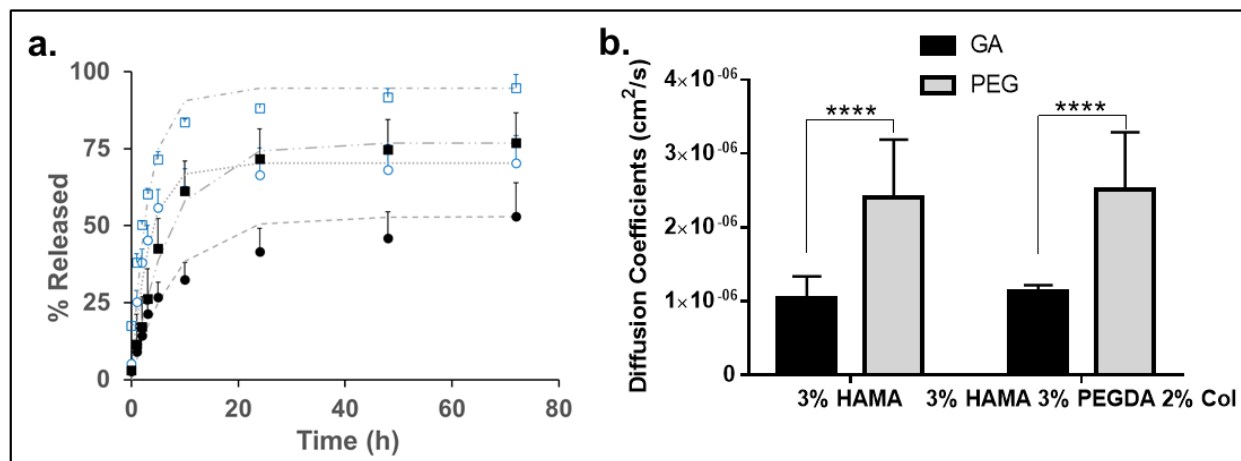


Figure 6. Mathematical modeling of diffusion coefficients. **a)** Experimental (markers) data and theoretical (dashed lines) model fit for the release profiles of GA (●) and PEG (○) in 3% HAMA and GA (■) and PEG (□) in 3% HAMA 3% PEGDA 2% Col reservoir models. **b)** Comparison between diffusion coefficients of GA and PEG in 3% HAMA and 3% HAMA 3% PEGDA 2% Col reservoir models show that PEG has a larger diffusion coefficient than GA in both models (**** $p < 0.0001$).

Table 1. Diffusion coefficients calculated for GA and PEG released in the various reservoir models.

<i>Compound Injected</i>	<i>Reservoir Model</i>	<i>D (cm²/s x 10⁷)</i>
GA	3% HAMA	10.4 ± 3.03
	3% HAMA 1% Col	6.29 ± 1.16
	3% HAMA 3% PEGDA 2% Col	11.3 ± 0.91
PEG	3% HAMA	24.0 ± 7.85
	3% HAMA 1% Col	26.3 ± 6.67
	3% HAMA 3% PEGDA 2% Col	25.2 ± 7.71

e) *Ex vivo* intratumoral release and fluorescent imaging

AT84 head and neck tumors were induced in mice and were resected 21 days later, then immediately injected to begin the *ex vivo* transport study (**Figure 7a**). Resected tumors were weighed and distributed between the GA and PEG injection groups so that the difference in average weight between the groups was negligible (**Figure 7b**). The release profile of GA and PEG in tumors *ex vivo* is shown in **Figure 7c**. PEG released significantly faster than GA, especially at the end of the release studies (**Figure 7d**). **Figure 7e** overlaps the release profiles of the HN tumors and that of the 3% HAMA reservoir gels. Despite being performed in slightly different experimental set-ups, this reservoir model mimicked the *ex vivo* release very well for GA while being slightly too fast for the earlier times of PEG.

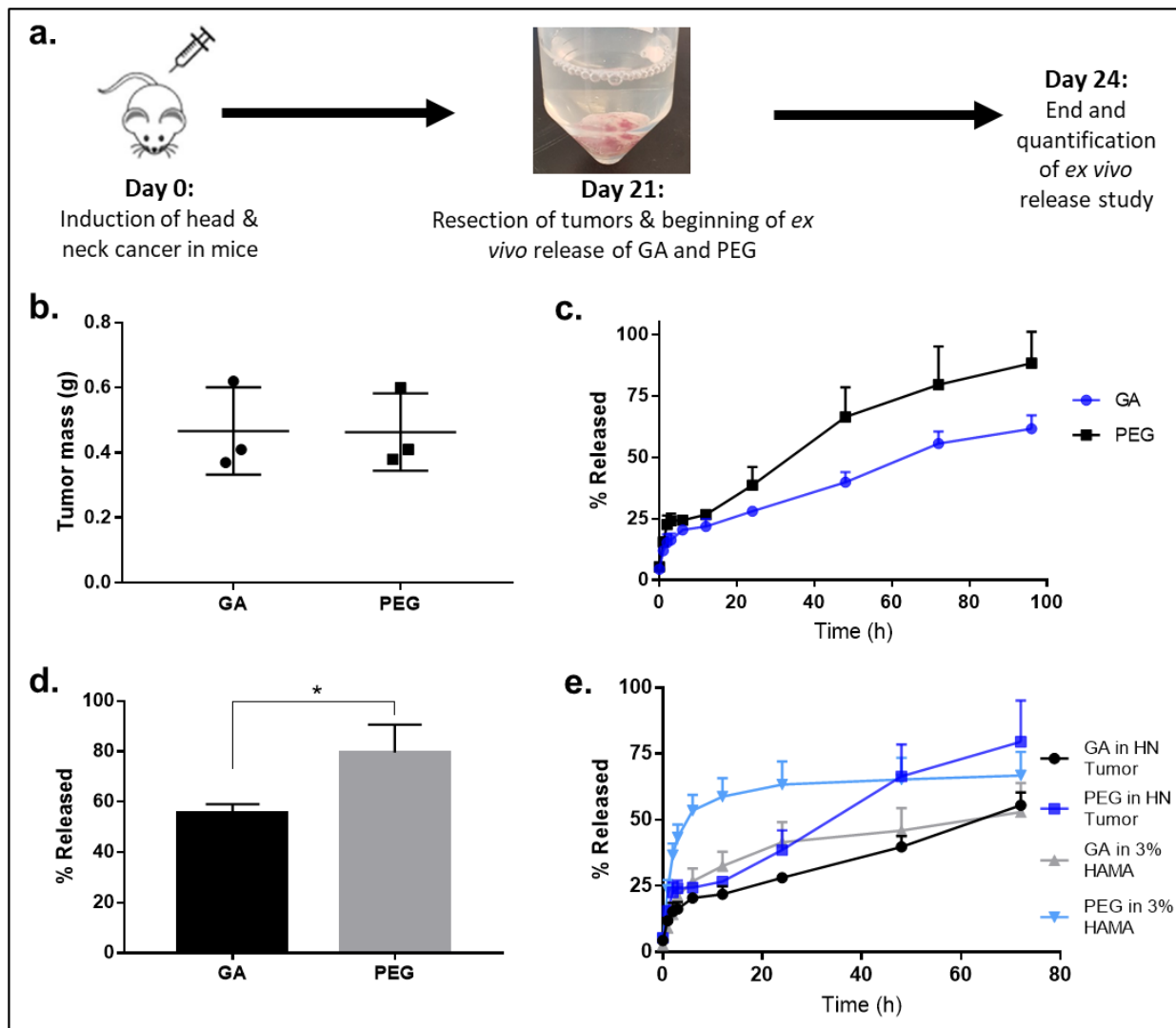


Figure 7. *Ex vivo* intratumoral release from tumors. **a)** Schematic of the induction and resection of tumors in mice and the *ex vivo* release. **b)** Mass distribution of tumors injected with GA and PEG. **c)** *Ex vivo* release of GA and PEG from the tumors. **d)** Comparison of the release rate of GA and PEG in the tumors after 72h. **e)** Comparison of release profiles of GA and PEG in the tumors and in the 3% HAMA reservoir models (n = 3 replicates per group, *p < 0.05).

A whole-body imager was used to track the transport of GA and PEG in tumors and fluorescent images were periodically acquired (**Figure 8**). The 3% HAMA reservoir models injected with GA and PEG were also fluorescently imaged (**Figure 8a**). GA exhibited more intense fluorescence over time in comparison to PEG, both in the tumors injected *ex vivo* as well as the ones injected *in vivo* and resected afterwards, respectively (**Figure 8b-c**). Overall, the findings of

the imaging and release studies indicate GA stays longer at the injection site and that this phenomenon can be modeled *in vitro* using reservoir gels.

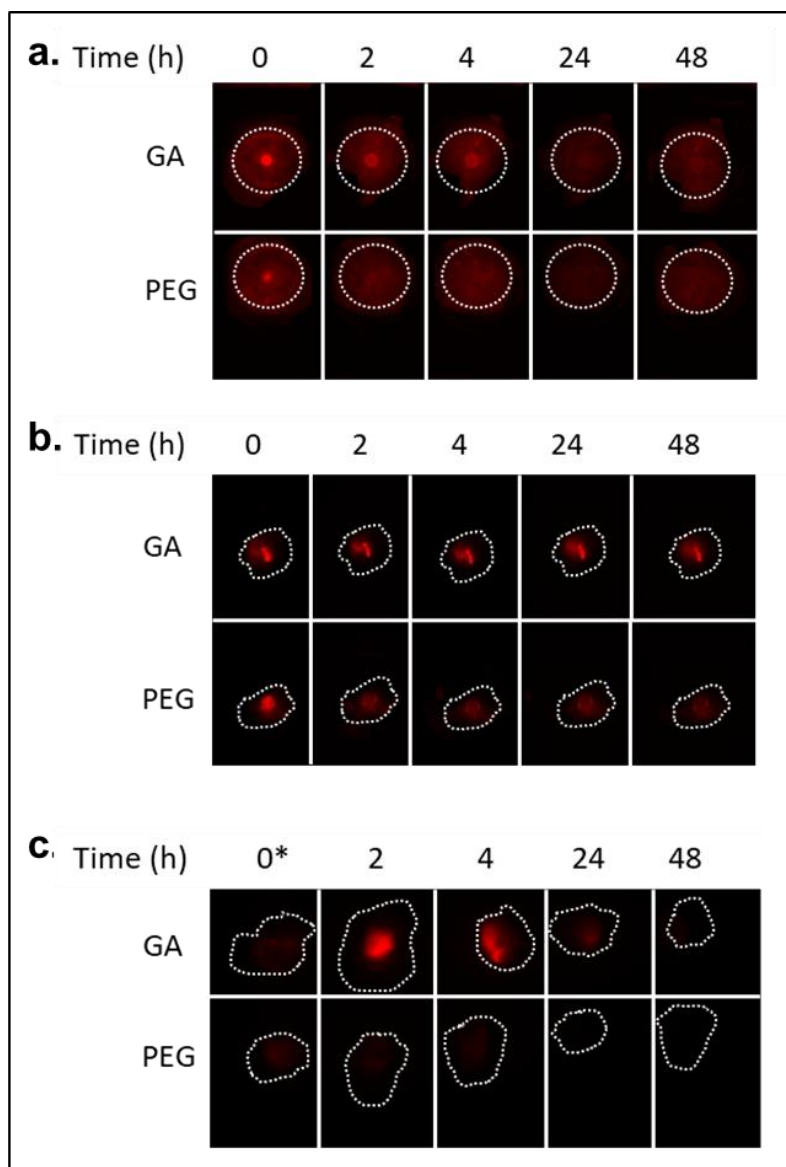


Figure 8. Fluorescent imaging of tumors and reservoir gels. **a)** Fluorescent images through time of 3% HAMA reservoir model gels injected with GA and PEG show better retention of GA than PEG in the gels. **b)** Fluorescent images through time of tumors injected with GA and PEG *ex vivo* show better retention of GA than PEG in tumors. **c)** Fluorescent images of tumors injected with GA and PEG *in vivo* and resected at the respective timepoints also show better retention of GA than PEG in tumors left *in vivo* until imaging. *Quenching was observed in the tumor of 0 h injected with GA *in vivo*.

4. Discussion

Hydrogels were designed to mimic biophysical properties of tumors and to study *in vitro* the drug release profiles of compounds administered intratumorally. To the best of our knowledge, the use of hydrogels to model an IT injection site has not been explored before. HA was selected because it is a major component of the ECM and TME and due to its optimal viscosity to simulate an injection site throughout the crosslinking process. Collagen I fibers were added to study the effect of the characteristic fibrotic regions in tumors (**Figure 1**), and PEGDA was used as a non-charged additive to deduce the effect of HA charge.

*Levental et al.*⁶⁶ showed that mammary glands at the invasive cancer stage are much stiffer (0.9-1.2 kPa average elastic modulus, G') than premalignant (~0.2 kPa average G') or normal (~0.1 kPa average G') mammary tissue via shear rheology. *Madsen et al.*⁸⁰ compared the relative stiffness of 4T1 mammary tumors with that of normal mammary tissue in mice using shear rheology and reported tumor G' values between 1 and 5 kPa. Their normal tissue G' was under 0.5 kPa so they demonstrated that the tumors were stiffer, but high variability in tumor G' was observed and their values were in a similar range to the G' measured in this study. In this study, the head and neck solid tumors displayed variable stiffness when analyzed under shear rheology (**Figure 2**), with an average G' of roughly 6 kPa but one of the tumors showing a stiffness as low as 2 kPa and another one as high as 9.7 kPa. Higher collagen density of the tumors correlated with a higher stiffness, as hypothesized and shown with Aniline Blue staining. HA hydrogels' stiffness was lower, so collagen I fibers were incorporated to both mimic the heterogeneous fibrotic regions in solid tumors and tune the matrix stiffness to approach that of tumor tissue. The addition of collagen I fibers and PEGDA to the HA scaffolds increased the G' by contributing to the

crosslinking network in the case of PEGDA, or by acting as a physical filler in the case of the collagen fibers.

Three dimensional scaffold tumor models have been used in previous papers for drug screening by assessing the apoptotic response of cultured cells and tumoroids to anticancer drugs.^{39, 52-54} In the work reported here, biophysical features of tumors that affect drug transport were incorporated into a scaffold model of IT injection rather than solely focusing on cell viability. Dispersed models (**Figure 4**) showed that GA, which has a pI ~10 due to prevalence of lysine, transported more slowly than PEG due to electrostatic interactions with HA in the matrix. Reservoir models, which more accurately mimic an injection site (**Figure 5**), exhibited release profiles that more closely mimicked tumor transport.

Addition of collagen I fibers hindered the electrostatic interactions of GA with HA, resulting in a faster release than that of the HAMA-only model. In the case of PEG, however, the release was unaffected by the addition of collagen fibers. This finding suggests that collagen-dense fibrous regions characteristic of tumors does not significantly affect the intratumoral retention of some therapies but may work against the retention of therapies that target other biopolymers within the TME. When PEGDA was added to the models, the release of GA became faster suggesting that for therapeutic agents that bind to a specific element in the TME, the other polymers present would hinder electrostatic interactions.

*Watkins et al.*⁸¹ studied the transport of fluorescent probes in photo crosslinked PEG hydrogels and computed diffusion coefficients for them. In this study, the faster diffusion rate of PEG compared to GA was also quantified with mathematically modeled diffusion coefficients for the reservoir models (**Figure 6, Table 1**) that support the previous findings and may facilitate

predictions of tumor transport for a variety of compound types. The diffusion coefficients calculated here are smaller than those found by *Watkins et al.*,⁸¹ which is expected considering that the dyes they tested had a smaller molecular weight and did not interact with the neutrally charged PEG hydrogels and thus diffused much faster than the GA and PEG tested in the HA hydrogels. Both the dispersed and the reservoir models predicted a slower rate for GA compared to PEG release from tumors when injected *ex vivo* (**Figure 7**) or *in vivo* (**Figure 8**). One particular reservoir model approximated the *ex vivo* release, but tumor transport is expected to change depending of the type solid tumor being injected. Certain tumors, for example, might display higher fibrosis and thus different IT retention, and it has been shown that gels used to model IT injection reported here can be tuned to account for such differences and the effect of more fibrous regions on drug transport can be emulated *in vitro*.

5. Conclusions

Hydrogels were designed to serve as a tumor tissue-mimicking biomaterial to model *in vitro* the intratumoral retention of IT injected therapeutic agents, an application of hydrogels not previously explored. The stiffness of HA scaffolds was tuned with collagen I fibers to mimic the dense fibrotic regions in tumors and model their bulk mechanical properties. GA and PEG of similar molecular weight were studied as model compounds administered intratumorally because of their different interactions with tumor extracellular matrix. Dispersed and reservoir injection models showed that GA has a higher IT retention than PEG due to electrostatic interaction between GA and the hyaluronic acid present in the tumor microenvironment. *Ex vivo* release studies and fluorescent imaging in murine head and neck tumors verified this phenomenon. A reservoir hydrogel successfully emulated an IT injection site, predicted that one compound would exhibit prolonged IT retention, and discerned the effect of variable tumor fibrosis on drug release rate.

Diffusion coefficients were calculated from mathematical models of drug release and serve as a predictive tool for extrapolating this work to other tumor scaffold structures or drug types. As IT therapies continue to emerge as an alternative to avoid the many side effects of systemic chemotherapeutics, this hydrogel platform may aid in the screening and selection of compounds for clinical trials.

Chapter 3: Conclusions and future directions

1. Conclusions and challenges

A tumor tissue-mimicking biomaterial to model *in vitro* the IT retention of therapeutic agents was designed using HA hydrogels. The development of a protocol to properly methacrylate HA took a few weeks, and the process from powder HA to lyophilized HAMA takes around two weeks so batches of 2 g were synthesized at a time. Adding collagen fibers to the model was inspired on previous work done on fiber-reinforced composites, and rheology was chosen as the technique to mechanically characterize the hydrogels and tumor tissue due to the viscoelastic nature of both.

Dispersed models were first used to get a preliminary idea of how differently GA and PEG interact with the designed scaffolds. Then, exploiting the potential of 3D printing, an injector was customized so that the hydrogels could be injected precisely in the center. Viscosity of the uncrosslinked scaffolds is a key parameter for the use of hydrogels as injection site simulators, and this was ensured by using 1 MDa HAMA. PEGDA alone was not viscous in solution, so it could only be used in tandem with HAMA for reservoir models. However, for dispersed models, PEGDA alone was possible since the injection site simulation was not desired. Mathematical modeling of diffusion in the models added a computational portion to this work that further characterized and quantified the predictive potential of the biomaterial. This was an enjoyable way of using the engineering and mathematics background obtained through undergraduate training.

One of the main challenges encountered in this project was finding chemically sound methods of quantification of the compounds being injected in the gels and intratumorally, both *ex vivo* and *in vivo*. Hydrogels degrade through time in a solution such as the physiological buffer. Despite it not being conspicuous, some of the HAMA that degraded through time and solubilized

into the buffer was being detected when the timepoints were analyzed using the BCA assay, which is widely used in protein research for determination of protein concentration. Thus, in response to this challenge, GA and PEG had to be chemically modified with rhodamine B to be able to detect their released amounts through fluorescence instead of absorbance. When injected into the tumor tissue, a similar challenge presented itself. The wavelength for Rhodamine B overlapped with autofluorescence of the tumor tissue, so the compounds were labelled with Sulfo-Cyanine7 to quantify them at a different wavelength that would not have interference from the HN tumors throughout the release studies. Therefore, even though the release studies were performed similarly, and the fluorescence readings were done with the same instrument, a dye different than that used for the *in vitro* release had to be used for the *ex vivo* release and the tumor imaging.

2. Future directions and applications

After characterizing of the biomaterial and proving its ability to work as a platform to model *in vitro* the intratumoral retention and some bulk biomechanical properties of solid tumors, as done in Chapter 2, the next step is to assess the scaffold's biocompatibility so that cancer cells can be 3D-cultured and the anticancer effect of the IT therapies can be screened by quantifying the resulting apoptosis.

a) Cancer cell encapsulation for 3D-culture

MDA-1986 head and neck squamous cell carcinoma (HNSCC) cells were kindly provided by Dr. Laird Forrest (University of Kansas Department of Pharmaceutical Chemistry). These cells were suspended in DMEM media with 10% fetal bovine serum (FBS) and 1% pen strep. The cells were then seeded on 100uL of 3% HAMA solution in a 24-well plate and dispersed homogeneously. The plate was centrifuged at 200 rpm for 1 minute and exposed to 365nm wavelength for 50 seconds in a UVP Transilluminator (Analytik Jena AG, Germany). After

crosslinking, the gels were covered with 0.5 mL of DMEM media and incubated for 4 days before performing the viability assays.

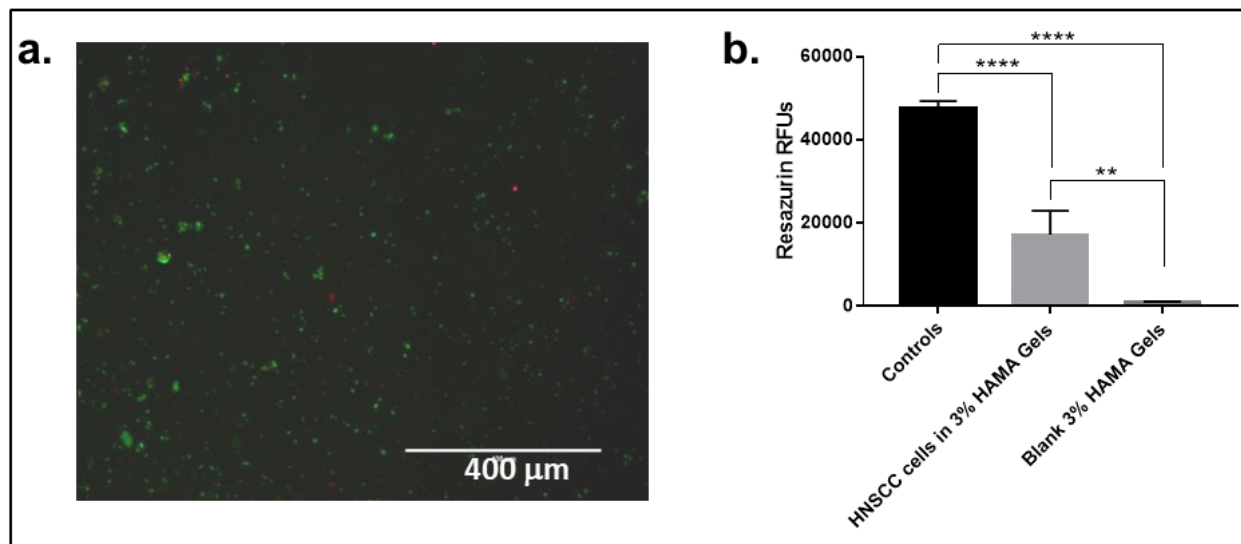


Figure 1. Cancer cells viability. **a)** Live-Dead assay of HNSCC cancer cells 3D-cultured in 3% HAMA hydrogels showing biocompatibility. **b)** Resazurin assay to determine the biochemical activity of 3D-cultured HNSCC in 3% HAMA hydrogels in comparison to blank gels and relative to 2D-cultured cells on a well-plate as controls (n = 3 replicates per group, **p < 0.01, ****p < 0.0001).

b) Assessment of cell viability

Cell viability in the 3% HAMA hydrogels was assessed via live/dead and resazurin assays (**Fig. 1**). **Fig. 1a** shows there are a lot more live (green) HNSCC cancer cells cultured in the 3% HAMA hydrogels than dead ones (red). Fluorescent images of the live-dead assay were obtained using the EVOS[®] FL Auto Imaging System from ThermoFisher Scientific. Resazurin assay was performed to determine the biochemical activity of 3D-cultured HNSCC in 3% HAMA hydrogels in comparison to blank gels and relative to 2D-cultured cells on a well-plate as controls (**Fig. 1b**). Significantly higher biochemical activity was observed in the HNSCC cells 3D-cultured in the HAMA gels in comparison to blank gels, but it was still lower than that observed in 2D-culture. This is probably because the UV-curing process is killing some cells, suggesting that the

crosslinking process can be optimized in order to enhance the biocompatibility of the scaffolds. Nonetheless, biocompatibility was demonstrated as a preliminary proof that the model designed can be further developed into a comprehensive *in vitro* tumor model to study IT therapeutics considering IT retention, fibrotic regions, and bulk tumor biomechanical properties.

c) Future applications and considerations

Based on the preliminary biocompatibility findings, we believe the model described can be used to 3D-culture cancer cells along with fibroblasts and immune cells, to more accurately represent the variety of cells found in solid tumors. Once the tumor's cellular components are incorporated, the *in vitro* IT injections can be performed inside a biological hood under sterile conditions, followed by delicate curing and then the release studies. This would allow for a much more complex modeling of IT delivery. After IT injection and release, the cells can be analyzed for apoptosis as a response to the therapeutic. Furthermore, the remaining alive cells can also be extracted from the scaffold and additional tests could be run in order to further study the therapeutic effects of the compound administered intratumorally. The viscosity associated with the HAMA solution could also be exploited for applications that incorporate 3D printing. In previous experiments, we saw that 7% HAMA solution was viscous enough to give good printing fidelity in a 3D BioPlotter, and the structure could be cured layer-by-layer by exposing it to UV 365 nm light while printing. Therefore, we believe that this model could be expanded even further by designing complex structures via 3D printing.

References

1. Marabelle, A.; Andtbacka, R.; Harrington, K.; Melero, I.; Leidner, R.; de Baere, T.; Robert, C.; Ascierto, P. A.; Baurain, J.-F.; Imperiale, M.; Rahimian, S.; Tersago, D.; Klumper, E.; Hendriks, M.; Kumar, R.; Stern, M.; Öhrling, K.; Massacesi, C.; Tchakov, I.; Tse, A.; Douillard, J.-Y.; Tabernero, J.; Haanen, J.; Brody, J., Starting the fight in the tumor: expert recommendations for the development of human intratumoral immunotherapy (HIT-IT). *Annals of Oncology* **2018**, *29* (11), 2163-2174.
2. Milling, L.; Zhang, Y.; Irvine, D. J., Delivering safer immunotherapies for cancer. *Advanced Drug Delivery Reviews* **2017**, *114*, 79-101.
3. Marabelle, A.; Kohrt, H.; Caux, C.; Levy, R., Intratumoral Immunization: A New Paradigm for Cancer Therapy. *Clinical Cancer Research* **2014**, *20* (7), 1747-1756.
4. Marabelle, A.; Tselikas, L.; de Baere, T.; Houot, R., Intratumoral immunotherapy: using the tumor as the remedy. *Annals of Oncology* **2017**, *28* (suppl_12), xii33-xii43.
5. Al-Hajj, M.; Wicha, M. S.; Benito-Hernandez, A.; Morrison, S. J.; Clarke, M. F., Prospective identification of tumorigenic breast cancer cells. *Proceedings of the National Academy of Sciences of the United States of America* **2003**, *100* (7), 3983-8.
6. Jenkins, R. W.; Barbie, D. A.; Flaherty, K. T., Mechanisms of resistance to immune checkpoint inhibitors. *British Journal Of Cancer* **2018**, *118*, 9.
7. Zhan, W.; Alamer, M.; Xu, X. Y., Computational modelling of drug delivery to solid tumour: Understanding the interplay between chemotherapeutics and biological system for optimised delivery systems. *Advanced Drug Delivery Reviews* **2018**, *132*, 81-103.
8. Shamsi, M.; Saghafian, M.; Dejam, M.; Sanati-Nezhad, A., Mathematical Modeling of the Function of Warburg Effect in Tumor Microenvironment. *Scientific Reports* **2018**, *8* (1), 8903.
9. Heldin, C.-H.; Rubin, K.; Pietras, K.; Östman, A., High interstitial fluid pressure — an obstacle in cancer therapy. *Nature Reviews Cancer* **2004**, *4*, 806.
10. Junttila, M. R.; de Sauvage, F. J., Influence of tumour micro-environment heterogeneity on therapeutic response. *Nature* **2013**, *501*, 346.
11. Gerweck, L. E.; Kozin, S. V.; Stocks, S. J., The pH partition theory predicts the accumulation and toxicity of doxorubicin in normal and low-pH-adapted cells. *British Journal Of Cancer* **1999**, *79*, 838.
12. Payen, V. L.; Porporato, P. E.; Baselet, B.; Sonveaux, P., Metabolic changes associated with tumor metastasis, part 1: tumor pH, glycolysis and the pentose phosphate pathway. *Cellular and Molecular Life Sciences* **2016**, *73* (7), 1333-1348.
13. Estrella, V.; Chen, T.; Lloyd, M.; Wojtkowiak, J.; Cornell, H. H.; Ibrahim-Hashim, A.; Bailey, K.; Balagurunathan, Y.; Rothberg, J. M.; Sloane, B. F.; Johnson, J.; Gatenby, R. A.; Gillies, R. J., Acidity Generated by the Tumor Microenvironment Drives Local Invasion. *Cancer Research* **2013**, *73* (5), 1524-1535.
14. Kareva, I.; Hahnfeldt, P., The Emerging “Hallmarks” of Metabolic Reprogramming and Immune Evasion: Distinct or Linked? *Cancer Research* **2013**, *73* (9), 2737-2742.
15. Sriraman, S. K.; Aryasomayajula, B.; Torchilin, V. P., Barriers to drug delivery in solid tumors. *Tissue barriers* **2014**, *2*, e29528-e29528.
16. Vinay, D. S.; Ryan, E. P.; Pawelec, G.; Talib, W. H.; Stagg, J.; Elkord, E.; Lichtor, T.; Decker, W. K.; Whelan, R. L.; Kumara, H. M. C. S.; Signori, E.; Honoki, K.; Georgakilas, A. G.; Amin, A.; Helferich, W. G.; Boosani, C. S.; Guha, G.; Ciriolo, M. R.; Chen, S.; Mohammed, S.

- I.; Azmi, A. S.; Keith, W. N.; Bilsland, A.; Bhakta, D.; Halicka, D.; Fujii, H.; Aquilano, K.; Ashraf, S. S.; Nowsheen, S.; Yang, X.; Choi, B. K.; Kwon, B. S., Immune evasion in cancer: Mechanistic basis and therapeutic strategies. *Seminars in Cancer Biology* **2015**, *35*, S185-S198.
17. Gabrilovich, D., Mechanisms and functional significance of tumour-induced dendritic-cell defects. *Nature Reviews Immunology* **2004**, *4* (12), 941-952.
18. Binnewies, M.; Roberts, E. W.; Kersten, K.; Chan, V.; Fearon, D. F.; Merad, M.; Coussens, L. M.; Gabrilovich, D. I.; Ostrand-Rosenberg, S.; Hedrick, C. C.; Vonderheide, R. H.; Pittet, M. J.; Jain, R. K.; Zou, W.; Howcroft, T. K.; Woodhouse, E. C.; Weinberg, R. A.; Krummel, M. F., Understanding the tumor immune microenvironment (TIME) for effective therapy. *Nature Medicine* **2018**, *24* (5), 541-550.
19. Xenaki, K. T.; Oliveira, S.; van Bergen En Henegouwen, P. M. P., Antibody or Antibody Fragments: Implications for Molecular Imaging and Targeted Therapy of Solid Tumors. *Front Immunol* **2017**, *8*, 1287-1287.
20. Jain, R. K., Barriers to Drug Delivery in Solid Tumors. *Scientific American* **1994**, *271* (1), 58-65.
21. Hobbs, S. K.; Monsky, W. L.; Yuan, F.; Roberts, W. G.; Griffith, L.; Torchilin, V. P.; Jain, R. K., Regulation of transport pathways in tumor vessels: Role of tumor type and microenvironment. *Proceedings of the National Academy of Sciences* **1998**, *95* (8), 4607.
22. Milosevic, M. F.; Fyles, A. W.; Wong, R.; Pintilie, M.; Kavanagh, M.-C.; Levin, W.; Manchul, L. A.; Keane, T. J.; Hill, R. P., Interstitial fluid pressure in cervical carcinoma. *Cancer* **1998**, *82* (12), 2418-2426.
23. Jain, R. K., Transport of Molecules in the Tumor Interstitium: A Review. *Cancer Research* **1987**, *47* (12), 3039-3051.
24. Fang, J.; Nakamura, H.; Maeda, H., The EPR effect: Unique features of tumor blood vessels for drug delivery, factors involved, and limitations and augmentation of the effect. *Advanced Drug Delivery Reviews* **2011**, *63* (3), 136-151.
25. Tong, R. T.; Boucher, Y.; Kozin, S. V.; Winkler, F.; Hicklin, D. J.; Jain, R. K., Vascular Normalization by Vascular Endothelial Growth Factor Receptor 2 Blockade Induces a Pressure Gradient Across the Vasculature and Improves Drug Penetration in Tumors. *Cancer Research* **2004**, *64* (11), 3731.
26. Winkler, F.; Kozin, S. V.; Tong, R. T.; Chae, S.-S.; Booth, M. F.; Garkavtsev, I.; Xu, L.; Hicklin, D. J.; Fukumura, D.; di Tomaso, E.; Munn, L. L.; Jain, R. K., Kinetics of vascular normalization by VEGFR2 blockade governs brain tumor response to radiation: Role of oxygenation, angiopoietin-1, and matrix metalloproteinases. *Cancer Cell* **2004**, *6* (6), 553-563.
27. Jain, R. K., Normalizing tumor vasculature with anti-angiogenic therapy: A new paradigm for combination therapy. *Nature Medicine* **2001**, *7* (9), 987-989.
28. Michel, C. C.; Curry, F. E., Microvascular Permeability. *Physiological Reviews* **1999**, *79* (3), 703-761.
29. Hashizume, H.; Baluk, P.; Morikawa, S.; McLean, J. W.; Thurston, G.; Roberge, S.; Jain, R. K.; McDonald, D. M., Openings between defective endothelial cells explain tumor vessel leakiness. *Am J Pathol* **2000**, *156* (4), 1363-1380.
30. McKee, T. D.; Grandi, P.; Mok, W.; Alexandrakis, G.; Insin, N.; Zimmer, J. P.; Bawendi, M. G.; Boucher, Y.; Breakefield, X. O.; Jain, R. K., Degradation of Fibrillar Collagen in a Human Melanoma Xenograft Improves the Efficacy of an Oncolytic Herpes Simplex Virus Vector. *Cancer Research* **2006**, *66* (5), 2509.

31. Stylianopoulos, T.; Munn, L. L.; Jain, R. K., Reengineering the Physical Microenvironment of Tumors to Improve Drug Delivery and Efficacy: From Mathematical Modeling to Bench to Bedside. *Trends Cancer* **2018**, *4* (4), 292-319.
32. Grantab, R.; Sivananthan, S.; Tannock, I. F., The Penetration of Anticancer Drugs through Tumor Tissue as a Function of Cellular Adhesion and Packing Density of Tumor Cells. *Cancer Research* **2006**, *66* (2), 1033.
33. Minchinton, A. I.; Tannock, I. F., Drug penetration in solid tumours. *Nature Reviews Cancer* **2006**, *6* (8), 583-592.
34. Huai, Y.; Hossen, M. N.; Wilhelm, S.; Bhattacharya, R.; Mukherjee, P., Nanoparticle Interactions with the Tumor Microenvironment. *Bioconjugate Chemistry* **2019**, *30* (9), 2247-2263.
35. Thurber, G. M.; Schmidt, M. M.; Wittrup, K. D., Antibody tumor penetration: Transport opposed by systemic and antigen-mediated clearance. *Advanced Drug Delivery Reviews* **2008**, *60* (12), 1421-1434.
36. Goodman, T. T.; Chen, J.; Matveev, K.; Pun, S. H., Spatio-temporal modeling of nanoparticle delivery to multicellular tumor spheroids. *Biotechnology and Bioengineering* **2008**, *101* (2), 388-399.
37. Varkhede, N.; Forrest, L., Understanding the Monoclonal Antibody Disposition after Subcutaneous Administration using a Minimal Physiologically based Pharmacokinetic Model. *J Pharm Pharm Sci* **2018**, *21* (1s), 130s-148s.
38. Sreepadmanabh, M.; Toley, B. J., Investigations into the cancer stem cell niche using in-vitro 3-D tumor models and microfluidics. *Biotechnology Advances* **2018**, *36* (4), 1094-1110.
39. Brancato, V.; Oliveira, J. M.; Correlo, V. M.; Reis, R. L.; Kundu, S. C., Could 3D models of cancer enhance drug screening? *Biomaterials* **2020**, *232*, 119744.
40. Pauli, C.; Hopkins, B. D.; Prandi, D.; Shaw, R.; Fedrizzi, T.; Sboner, A.; Sailer, V.; Augello, M.; Puca, L.; Rosati, R.; McNary, T. J.; Churakova, Y.; Cheung, C.; Triscott, J.; Pisapia, D.; Rao, R.; Mosquera, J. M.; Robinson, B.; Faltas, B. M.; Emerling, B. E.; Gadi, V. K.; Bernard, B.; Elemento, O.; Beltran, H.; Demichelis, F.; Kemp, C. J.; Grandori, C.; Cantley, L. C.; Rubin, M. A., Personalized In Vitro and In Vivo Cancer Models to Guide Precision Medicine. *Cancer Discovery* **2017**, *7* (5), 462.
41. Skardal, A.; Mack, D.; Atala, A.; Soker, S., Substrate elasticity controls cell proliferation, surface marker expression and motile phenotype in amniotic fluid-derived stem cells. *Journal of the Mechanical Behavior of Biomedical Materials* **2013**, *17*, 307-316.
42. Riedl, A.; Schleder, M.; Pudelko, K.; Stadler, M.; Walter, S.; Unterleuthner, D.; Unger, C.; Kramer, N.; Hengstschläger, M.; Kenner, L.; Pfeiffer, D.; Krupitza, G.; Dolznig, H., Comparison of cancer cells in 2D vs 3D culture reveals differences in AKT–mTOR–S6K signaling and drug responses. *Journal of Cell Science* **2017**, *130* (1), 203.
43. Lu, P.; Weaver, V. M.; Werb, Z., The extracellular matrix: a dynamic niche in cancer progression. *J Cell Biol* **2012**, *196* (4), 395-406.
44. Gu, L.; Mooney, D. J., Biomaterials and emerging anticancer therapeutics: engineering the microenvironment. *Nature reviews. Cancer* **2016**, *16* (1), 56-66.
45. Ruedinger, F.; Lavrentieva, A.; Blume, C.; Pepelanova, I.; Scheper, T., Hydrogels for 3D mammalian cell culture: a starting guide for laboratory practice. *Applied Microbiology and Biotechnology* **2015**, *99* (2), 623-636.

46. Liu, Z.; Vunjak-Novakovic, G., Modeling tumor microenvironments using custom-designed biomaterial scaffolds. *Current Opinion in Chemical Engineering* **2016**, *11*, 94-105.
47. Thoma, C. R.; Stroebel, S.; Rösch, N.; Calpe, B.; Krek, W.; Kelm, J. M., A High-Throughput–Compatible 3D Microtissue Co-Culture System for Phenotypic RNAi Screening Applications. *Journal of Biomolecular Screening* **2013**, *18* (10), 1330-1337.
48. Lancaster, M. A.; Knoblich, J. A., Organogenesis in a dish: Modeling development and disease using organoid technologies. *Science* **2014**, *345* (6194), 1247125.
49. Clevers, H., Modeling Development and Disease with Organoids. *Cell* **2016**, *165* (7), 1586-1597.
50. Laurent, T. C.; Fraser, J. R. E., Hyaluronan1. *The FASEB Journal* **1992**, *6* (7), 2397-2404.
51. Toole, B. P., Hyaluronan: from extracellular glue to pericellular cue. *Nature Reviews Cancer* **2004**, *4* (7), 528-539.
52. Fong, E. L. S.; Martinez, M.; Yang, J.; Mikos, A. G.; Navone, N. M.; Harrington, D. A.; Farach-Carson, M. C., Hydrogel-Based 3D Model of Patient-Derived Prostate Xenograft Tumors Suitable for Drug Screening. *Molecular Pharmaceutics* **2014**, *11* (7), 2040-2050.
53. Xu, X.; Gurski, L. A.; Zhang, C.; Harrington, D. A.; Farach-Carson, M. C.; Jia, X., Recreating the tumor microenvironment in a bilayer, hyaluronic acid hydrogel construct for the growth of prostate cancer spheroids. *Biomaterials* **2012**, *33* (35), 9049-9060.
54. Ananthanarayanan, B.; Kim, Y.; Kumar, S., Elucidating the mechanobiology of malignant brain tumors using a brain matrix-mimetic hyaluronic acid hydrogel platform. *Biomaterials* **2011**, *32* (31), 7913-7923.
55. Lo, C. M.; Wang, H. B.; Dembo, M.; Wang, Y. L., Cell movement is guided by the rigidity of the substrate. *Biophys J* **2000**, *79* (1), 144-152.
56. Paszek, M. J.; Zahir, N.; Johnson, K. R.; Lakins, J. N.; Rozenberg, G. I.; Gefen, A.; Reinhart-King, C. A.; Margulies, S. S.; Dembo, M.; Boettiger, D.; Hammer, D. A.; Weaver, V. M., Tensional homeostasis and the malignant phenotype. *Cancer Cell* **2005**, *8* (3), 241-254.
57. Kolacna, L.; Bakesova, J.; Varga, F.; Kostakova, E.; Planka, L.; Necas, A.; Lukas, D.; Amler, E.; Pelouch, V., Biochemical and biophysical aspects of collagen nanostructure in the extracellular matrix. *Physiological research* **2007**, *56 Suppl 1*, S51-60.
58. Jodele, S.; Blavier, L.; Yoon, J. M.; DeClerck, Y. A., Modifying the soil to affect the seed: role of stromal-derived matrix metalloproteinases in cancer progression. *Cancer metastasis reviews* **2006**, *25* (1), 35-43.
59. Ramaswamy, S.; Ross, K. N.; Lander, E. S.; Golub, T. R., A molecular signature of metastasis in primary solid tumors. *Nature genetics* **2003**, *33* (1), 49-54.
60. Martin, L. J.; Boyd, N. F., Mammographic density. Potential mechanisms of breast cancer risk associated with mammographic density: hypotheses based on epidemiological evidence. *Breast Cancer Research* **2008**, *10* (1), 201.
61. Yamauchi, M.; Shiiba, M., Lysine hydroxylation and cross-linking of collagen. *Methods in molecular biology (Clifton, N.J.)* **2008**, *446*, 95-108.
62. Erler, J. T.; Bennewith, K. L.; Cox, T. R.; Lang, G.; Bird, D.; Koong, A.; Le, Q. T.; Giaccia, A. J., Hypoxia-induced lysyl oxidase is a critical mediator of bone marrow cell recruitment to form the premetastatic niche. *Cancer Cell* **2009**, *15* (1), 35-44.
63. van der Slot, A. J.; van Dura, E. A.; de Wit, E. C.; DeGroot, J.; Huizinga, T. W. J.; Bank, R. A.; Zuurmond, A.-M., Elevated formation of pyridinoline cross-links by profibrotic cytokines

- is associated with enhanced lysyl hydroxylase 2b levels. *Biochimica et Biophysica Acta (BBA) - Molecular Basis of Disease* **2005**, 1741 (1), 95-102.
64. Colpaert, C. G.; Vermeulen, P. B.; Fox, S. B.; Harris, A. L.; Dirix, L. Y.; Van Marck, E. A., The presence of a fibrotic focus in invasive breast carcinoma correlates with the expression of carbonic anhydrase IX and is a marker of hypoxia and poor prognosis. *Breast cancer research and treatment* **2003**, 81 (2), 137-47.
65. Colpaert, C.; Vermeulen, P.; Van Marck, E.; Dirix, L., The Presence of a Fibrotic Focus Is an Independent Predictor of Early Metastasis in Lymph Node-Negative Breast Cancer Patients. *The American Journal of Surgical Pathology* **2001**, 25 (12).
66. Levental, K. R.; Yu, H.; Kass, L.; Lakins, J. N.; Egeblad, M.; Erler, J. T.; Fong, S. F. T.; Csiszar, K.; Giaccia, A.; Wenginger, W.; Yamauchi, M.; Gasser, D. L.; Weaver, V. M., Matrix Crosslinking Forces Tumor Progression by Enhancing Integrin Signaling. *Cell* **2009**, 139 (5), 891-906.
67. Katt, M. E.; Placone, A. L.; Wong, A. D.; Xu, Z. S.; Searson, P. C., In Vitro Tumor Models: Advantages, Disadvantages, Variables, and Selecting the Right Platform. *Frontiers in bioengineering and biotechnology* **2016**, 4, 12-12.
68. Ridky, T. W.; Chow, J. M.; Wong, D. J.; Khavari, P. A., Invasive three-dimensional organotypic neoplasia from multiple normal human epithelia. *Nature Medicine* **2010**, 16 (12), 1450-1455.
69. Yi, H.-G.; Jeong, Y. H.; Kim, Y.; Choi, Y.-J.; Moon, H. E.; Park, S. H.; Kang, K. S.; Bae, M.; Jang, J.; Youn, H.; Paek, S. H.; Cho, D.-W., A bioprinted human-glioblastoma-on-a-chip for the identification of patient-specific responses to chemoradiotherapy. *Nature Biomedical Engineering* **2019**, 3 (7), 509-519.
70. Lu, S.; Cuzzucoli, F.; Jiang, J.; Liang, L.-G.; Wang, Y.; Kong, M.; Zhao, X.; Cui, W.; Li, J.; Wang, S., Development of a biomimetic liver tumor-on-a-chip model based on decellularized liver matrix for toxicity testing. *Lab Chip* **2018**, 18 (22), 3379-3392.
71. Lanz, H. L.; Saleh, A.; Kramer, B.; Cairns, J.; Ng, C. P.; Yu, J.; Trietsch, S. J.; Hankemeier, T.; Joore, J.; Vulto, P.; Weinsilboum, R.; Wang, L., Therapy response testing of breast cancer in a 3D high-throughput perfused microfluidic platform. *BMC Cancer* **2017**, 17 (1), 709.
72. Singh, A.; Brito, I.; Lammerding, J., Beyond Tissue Stiffness and Bioadhesivity: Advanced Biomaterials to Model Tumor Microenvironments and Drug Resistance. *Trends Cancer* **2018**, 4 (4), 281-291.
73. Song, J. Y.; Larson, N. R.; Thati, S.; Torres-Vazquez, I.; Martinez-Rivera, N.; Subelzu, N. J.; Leon, M. A.; Rosa-Molinar, E.; Schöneich, C.; Forrest, M. L.; Middaugh, C. R.; Berkland, C. J., Glatiramer acetate persists at the injection site and draining lymph nodes via electrostatically-induced aggregation. *Journal of Controlled Release* **2019**, 293, 36-47.
74. Meng, Q.; Yu, M.; Zhang, H.; Ren, J.; Huang, D., Synthesis and application of N-hydroxysuccinimidyl rhodamine B ester as an amine-reactive fluorescent probe. *Dyes and Pigments* **2007**, 73 (2), 254-260.
75. Zhao, X.; Lang, Q.; Yildirim, L.; Lin, Z. Y.; Cui, W.; Annabi, N.; Ng, K. W.; Dokmeci, M. R.; Ghaemmaghami, A. M.; Khademhosseini, A., Photocrosslinkable Gelatin Hydrogel for Epidermal Tissue Engineering. *Advanced healthcare materials* **2016**, 5 (1), 108-18.
76. Siepmann, J.; Siepmann, F., Modeling of diffusion controlled drug delivery. *Journal of controlled release : official journal of the Controlled Release Society* **2012**, 161 (2), 351-62.

77. Hier, M. P.; Black, M. J.; Shenouda, G.; Sadeghi, N.; Karp, S. E., A murine model for the immunotherapy of head and neck squamous cell carcinoma. *The Laryngoscope* **1995**, *105* (10), 1077-80.
78. Paolini, F.; Massa, S.; Manni, I.; Franconi, R.; Venuti, A., Immunotherapy in new pre-clinical models of HPV-associated oral cancers. *Hum Vaccin Immunother* **2013**, *9* (3), 534-543.
79. de Jong, S.; van Veen, T. A. B.; de Bakker, J. M. T.; van Rijen, H. V. M., Monitoring cardiac fibrosis: a technical challenge. *Neth Heart J* **2012**, *20* (1), 44-48.
80. Madsen, C. D.; Cox, T. R., Relative Stiffness Measurements of Tumour Tissues by Shear Rheology. *Bio-protocol* **2017**, *7* (9), e2265.
81. Watkins, A. W.; Anseth, K. S., Investigation of Molecular Transport and Distributions in Poly(ethylene glycol) Hydrogels with Confocal Laser Scanning Microscopy. *Macromolecules* **2005**, *38* (4), 1326-1334.